Potentiality of a velocity profiler to investigate sewers

Results of laboratory experiments

Juan Sebastián Cedillo Galarza

Technische Universiteit Delft

TU Delft Delft University of Technology

Challenge the future

POTENTIALITY OF A VELOCITY PROFILER TO INVESTIGATE SEWERS

RESULTS OF LABORATORY EXPERIMENTS

by

Juan Sebastián Cedillo Galarza

in partial fulfillment of the requirements for the degree of

Master of Science
in Water management

at the Delft University of Technology,
to be defended publicly on Monday August 15, 2016 at 9:00 AM.

Supervisor:	Dr. M. Lepot	TU Delft
Thesis committee:	Prof. dr. F. Clemens,	TU Delft
	Dr. W. Luxenburg,	TU Delft

An electronic version of this thesis is available at http://repository.tudelft.nl/.

TU Delft Delft University of Technology

TABLE OF CONTENTS

ABSTRACT

In order to propose a new sewer inspection method, a velocity/turbidity profiler (Ubertone, UB Flow F-315) has been tested in a laboratory. A 50 m glass flume has been adapted with several lateral connections (with a range of diameters, angles, intrusions, cracks), supplied by a 1 m3 tank. Placed just below the free surface on a rotating (to scan the wet section) and translating (along the main axe of the flume) structure, velocity profiles have been recorded and accurately positioned along the reach (with data from three laser distance meters and a 3 Mpix camera): a 3D cloud of raw velocities is created. After raw data pretreatment (deduction of translation velocity, Nyquist jumps correction), a five step-interpolation (adapted from [16]) method has been implemented and tested: i) data filtering, ii) transformation to flume coordinates velocities, iii) isotropic gridding, iv) anisotropic gridding and v) continuity correction. In order to perform the last step, two resolution schemes have been tested: staggered and non-staggered grid. With external CFD data, the first one shows its superiority (stability) on the second one and provide consistent results to data obtained from commercial CFD software. Despite the UB Flow provides good average data, its design and instantaneous velocities make it no suitable yet for field application.

Symbol	Description	Dimension/Unit
A,B	Vectors form by any two points of the reference triangle and the modified triangle	L/m
A_D	Discretization of convective term	-/-
a,b,c	Components OUT vector	L/m
a2,b2	Minor and major axis of the ellipse used for isotropic gridding	L/m
B_f	A fluid property	-/-
b_f	Amount of $B_f per unit of mass$	-/-
c_s	Sound speed	$\frac{L}{T}/\frac{m}{s}$
D_D	Discretization of viscous forces	-/-
E	Vertical position of measured data	L/m
fo	UB Flow Emission frequency	$\frac{1}{T}$/Hertz
G	Water consumption	$L^3 \cdot T^{-1} \cdot inhabitant^{-1}$ /$l \cdot d^{-1} \cdot inhabitant^{-1}$
G'	Wastewater generated	$L^3 \cdot T^{-1} \cdot inhabitant^{-1}$ /$l \cdot d^{-1} \cdot inhabitant^{-1}$
x	Return factor	-/-
i,j,k	Counters of pressure and velocity in x,y, and z	-/-
n	Current time step	T/s
n+1	One time step further in the time discretization	T/s
o	Coordinate origin according to laser plane	L/m
OUT	Vector component of R. R's 3rd row	$\frac{1}{L}/\frac{1}{m}$
P	Relative origin of UB flow measurement	L/m
P'	UB flow velocity measuring point Transducer 1 (no rotation)	L/m
P"	UB flow velocity measuring point Transducer 3 (no rotation)	L/m
PP'	UB flow velocity measuring point including rotation Transducer 1	L/m
PP"	UB flow velocity measuring point including rotation Transducer 3	L/m
PRF	Repetition frequency	$\frac{1}{T}$/Hertz
pc_{back}	Position of laser points according to back camera plane	L/m
p_{R2}	Position of laser points according to laser plane	L/m
p_{R1}	Vector to translate the coordinates of the modified triangle	L/m
Q	Point where tranducers beams has a common origin	L/m
Q'	Points where transducer beams has a common origin after rotation	L/m
R	Rotation Matrix	$\frac{1}{L}/\frac{1}{m}$
R3	Laser reference system	-/-
RIGHT	Vector component of R. R's 1st row	$\frac{1}{L}/\frac{1}{m}$
Rx	Rotation Matrix around x axes	L/m
Ry	Rotation Matrix around y axes	L/m
Rz	Rotation Matrix around z axes	L/m
R_3	Laser reference system	L/m
s_{back}	Coefficient to correct camera measurements	-/-
T	Translation Matrix	L/m
Tr	Matrix to transform from laser plane R_3 to back camera plane ψ_3	-/-
t	Time	T/s
U	Fluid velocity vector	$\frac{L}{T}/\frac{m}{s}$
U_x, U_y, U_z	Velocity components in x,y, and z direction	$\frac{L}{T}/\frac{m}{s}$
V_R	Reference velocity	$\frac{L}{T}/\frac{m}{s}$
V_{set-up}	Velocity of set-up during experiment	$\frac{L}{T}/\frac{m}{s}$
V_{TR1}	Flow velocity component in Transducer 1 direction	$\frac{L}{T}/\frac{m}{s}$

V_{TR3}	Flow velocity component in Transducer 3 direction	$\frac{L}{T}$ / $\frac{m}{s}$
V_{UB}	Flow velocity component in transducer direction	$\frac{L}{T}$ / $\frac{m}{s}$
V_{yUB}	Vertical component of velocity measured by UB flow	$\frac{L}{T}$ / $\frac{m}{s}$
x,y,z	Coordinates	L/m
x_i,y_i	x, y coordinate of laser R_3	
x_o,y_o	Center of ellipse and circle in a anisotropic and isotropic gridding	L/m
x_x	Return factor	-/-
α	Angle between U_x and U_y obtained during isotropic gridding	Angle/Radians
Δt	Time step	T/s
Δx	Space step in x direction	L/m
Δy	Space step in y direction	L/m
Δz	Space step in z direction	L/m
θ_x	Yaw angle of the set up	Angle/Radians
θ_y	Roll angle of the set up	Angle/Radians
θ_z	Pitch angle of the set up	Angle/Radians
μ	Dynamic viscosity	$\frac{M}{L \cdot T}$/Pa·s
υ	Cinematic viscocity	$\frac{L^2}{T}$
ρ	Water density	$\frac{M}{L^3}$
ϕ	Function depending on x	-/-
ψ	Back camera reference system	-/-

1

INTRODUCTION

Sewer systems are buried structures designed to transport wastewater and storm water: Two types of sewer systems exists (separate or combine).Waste water and storm water present different matrices and discharges that require different (pre) treatment process [1] that is why sewer systems are important for two main reasons:

1. **Sanitation** in order to avoid outbreaks due to the exposure of waterborne diseases
2. **Drainage** to prevent flooding problems on the catchment

Several failures may occur in a sewer pipe [2]: longitudinal cracks, circumferential cracks, roots, external pipeline build through the sewer wall or miss-connection. Detection of illicit/cross/mis-connection is the major concern for separate sewer diagnostic to avoid more frequent pollution and/or flooding [3].

In order to guarantee the continuity of sanitation service, two approaches are used: preventive or post failure repair, the first one being the most cost effective [4]. Therefore, inspection techniques are needed. Several methods are available to detect cross connections (Appendix A). Those methodologies are divided in three groups: Sensor Evaluation, Combination of sensors and Method using indicators. However, in general all those methodologies are able to detect cross connections under certain conditions only(The most common methodology is the use of CCTV cameras, but the detection depends on the quality image and technical person expertise). Detection is not a easy task due to the following reasons:

- their random nature and varying flow. The domestic discharge occurs in a time of 30 $\frac{minute}{person*day}$ [5]
- lack of personal for inspections
- lack of money to do the maintenance
- low reliability in the applied methodologies to detect it

The water sources in a sewer system are wastewater, storm water and infiltration/inflow. Wastewater generation is related with water consumption in domestic, commercial and industrial activities. Domestic consumption depends on human behavior. Both are linked with Equation 1.1 [1]:

$$G' = x_x \cdot G \tag{1.1}$$

Where:
G' wastewater generated (liter per capita per day)
G water consumption (liter per capita per day)
x_x return factor (-)

x_x is necessary since not all the water consumed returns to the sewer system. Moreover, the drinking water consumption is not fixed, but it follows a time pattern (yearly variation due to seasons and daily variations because of human activities). Commercial consumption of water suffers from lack of data. Industrial water consumption depends on industry production. Storm water is generated by rainfall in most of the cases

(Snow is a source of storm water as well). It is the result of transformation of rainfall to runoff, consequently its quality and quantity depends on catchment characteristics. Infiltration and inflow is an external source of water in the sewer system. This water enters into the system trough fissures, pipe joints, couplings and manholes. Its quantity is estimated in 0.01 to 1 m^3 per day per millimeter diameter per kilometer length [1].

In order to develop a new complete inspection method and as that following of [6], the FOULC (Fast Overall-scanning of Underground and Linear Constructions) project is now starting comprising the design, construction and test of multi sensor hovercraft drone. This device will be equipped with a laser, infrared camera (IR), sonar and velocity profiler. The laser is intended to detect wall losses due to biochemical corrosion and other objects. Infrared camera is used to detect the thermal print, find and quantify cross connections. Sonar is used to measure the sediment profile inside the pipe. The velocity/turbidity profiler measures the velocity distribution to detect and quantify cross , illicit connections and leakages. This last device (Ubertone,Ub flow F-315) is studied in this thesis.

Based on experimental (Scheldt Fume, Deltares) or CFD (Computational Fluid Dynamics) data, a complete method has been designed and tested: from the raw velocity profile to the final interpolated velocity distribution. The here after detailed steps imply, sensor calibration, 3D gridding and computer interpolation method based on the fractional step method.

2

MATERIALS AND METHODS

2.1. MATERIALS

2.1.1. TURBIDITY VELOCITY PROFILER

The velocity/turbidity profiler is able to measure velocity and turbidity profiles along two acoustic beams (Figure 2.1(a)) via two electronic transducers (Transducer 1, named TR1 and Transducer 3, named TR3). Ultrasonic waves are sent by *TR1*/*TR3* and , based on acoustic theories, the velocity and acoustic turbidity are derived from frequencies and the alteration of back scattered signal by particles or bubbles [7]. The data is measured within a cell (Part of the acoustic beam Figure 2.1(b)) with geometric characteristics given by Equation 2.1.

$$r_{em} = c_s \cdot \frac{n_{em}}{2f_o}; y_{em} = r_{em} \cdot \sin(\beta) \tag{2.1}$$

Where:
r_{em} cell thickness along the beam axis (m)
c_s sound speed (m/s)
n_{em} number of periods at the carrier frequency inside the emitted burst
f_o carrier frequency (Hz)].
y_{em} thickness of the measurement cell (m)
β angle of the transducer (Degrees)

Transducer 1 forms an angle of 65 degrees with the longitudinal plane of the device, while Transducer 3 forms an angle of 97 degrees with it (Figure 2.1(a)).

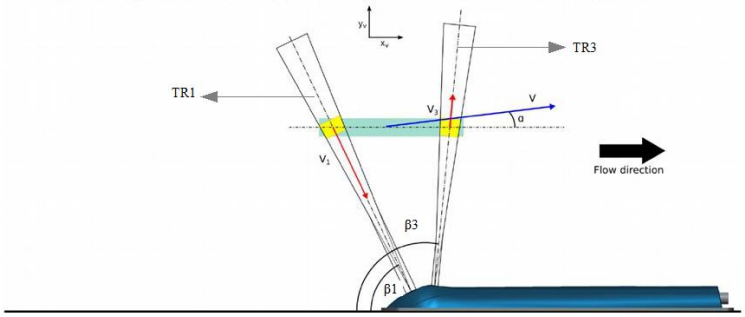

(a) UB flow velocity components

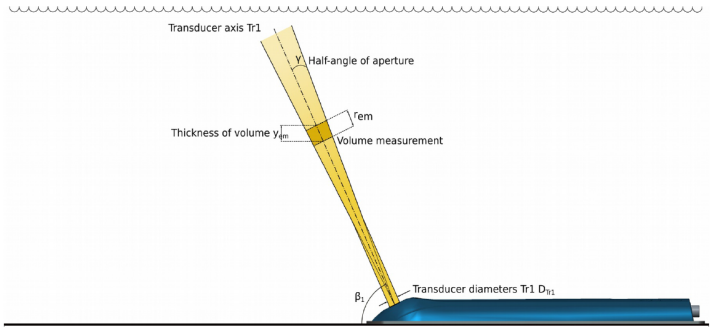

(b) Meusurement cell

Figure 2.1: Windows used during experiments

2.1.2. EXPERIMENTAL SET UP, FLUME AND ROTATION/TRANSLATION STRUCTURE

Figure 2.2 shows the set-up used by [6]: the one used in this thesis has been derived from it. [6] set-up consists on three lasers in parallel, a back camera, a reflective board, a front camera and a laser profiler.

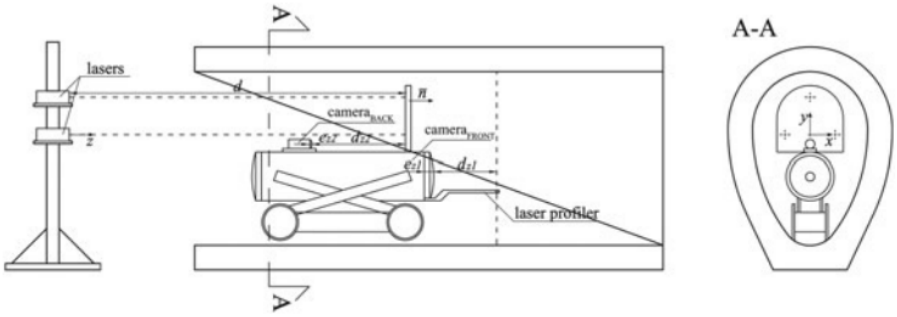

Figure 2.2: Set-up used in [6] (Image taken from [6])

The set-up used in the current experimental work has the following components (Figure 2.3):

Laser distance meters $[Dimetix, FLS-C10]$ Figure 2.4. Three laser distance meters measure the distances between the laser distance meter reference plane and the PVC plate (Figure 2.3).

Backcamera $[Allied\ Vision, Manta\ G\ 282]$ (Figure 2.5), which records with a frame rate of 12 frs the position of the lasers on the PVC plate.

Velocity/Turbidity profiler $[Ubertone\ UB\ flow, F-315]$ (Figure 2.1). Previously described.

Flume $[Scheldt]$ (Figure 2.6). This flume has a rectangular cross section (1.2 m depth by 1 m width). At the upstream part, flow rate is controlled by a pump. At downstream part, water level was control by a rectangular weir.

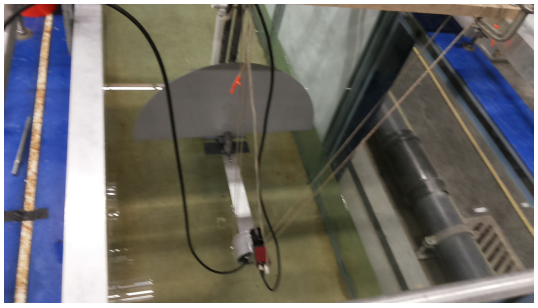

(a) Picture of the set up

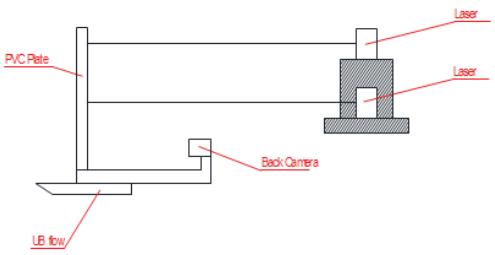

(b) Set up drawing

Figure 2.3: Set up Scheme

Figure 2.4: Laser

Figure 2.5: Back Camera

The hardware conception of the UB flow does not allow the simultaneous use of TR1 and TR3. This measurement is along a beam (the angle of the beam is the same as the transducer used). The obtained data in each measurement are single profiles only. In order to scan the entire wet section and the reach length, the UB flow was rotated and translated around along the z axes (Figure 2.7) toward the "lateral connection"resulting in a data sampling scheme similar to the one presented in Figure 2.8. Back camera and lasers took data at the same time as UB flow. However, the three laser distance meters and the camera/UB group were not connected to the same computer (i.e. acquisition system): that is why a synchronization was required. A dis-

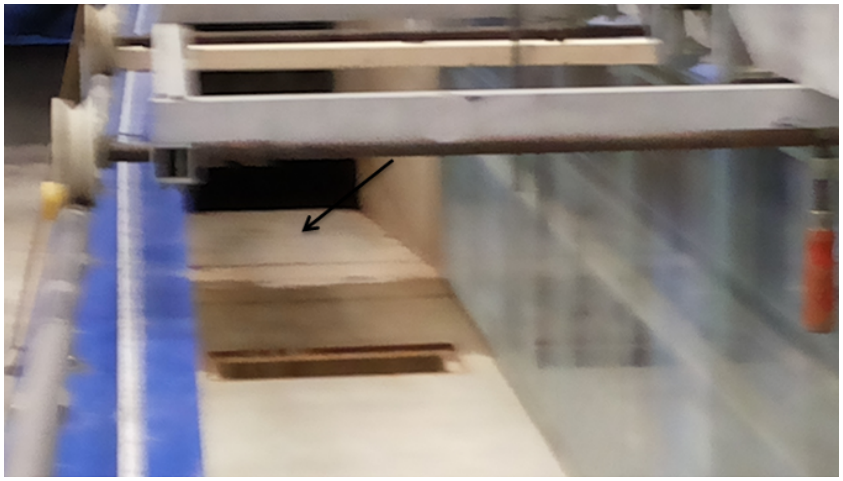

Figure 2.6: Flume water inlet

turbance (object placed on one laser beam) allow this synchronization: shorter distance (Figure 2.9(b)) and missing dot on the video (Figure 2.9(c)).

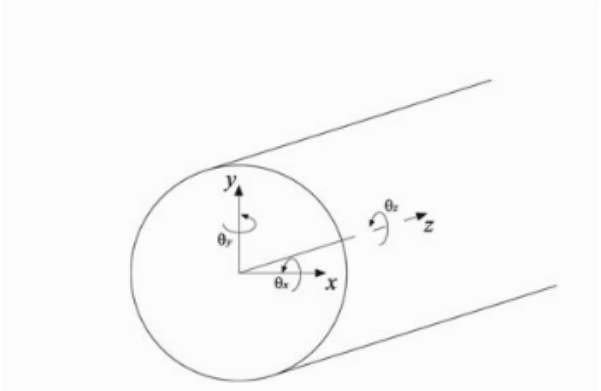

Figure 2.7: Left-handed coordinate system and Tait Bryan formalism (Image taken from [6])

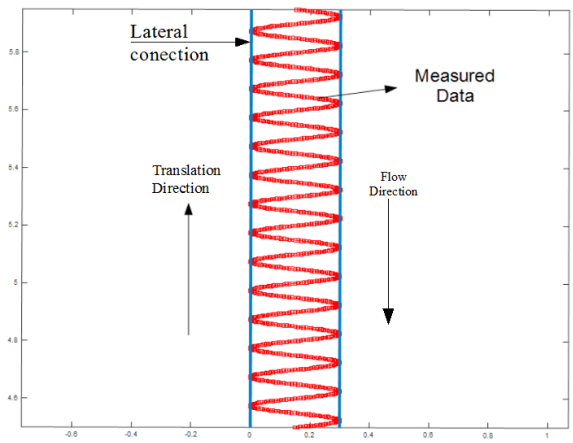

Figure 2.8: Scheme of measured data

In order to create various lateral connections several windows with different inlet types have been designed and installed along the flume. Figure 2.10 illustrates the windows disposition along the flume, while Figure 2.11 shows details of each window.

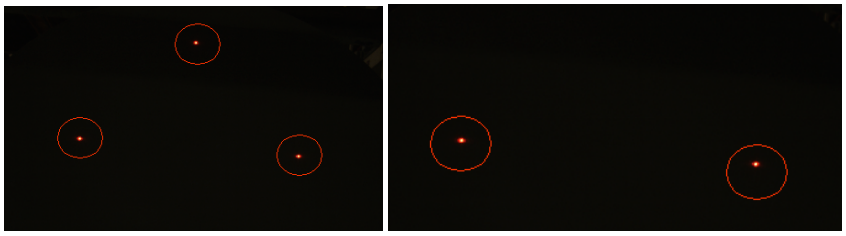

(a) Normal camera recording of three lasers

(b) Disturbance in the camera recording

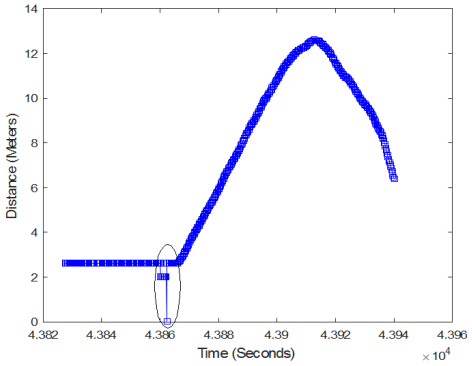

(c) Laser reading of disturbance

Figure 2.9: Camera laser synchronization

Figure 2.11(a) represents cross connections with different pipe diameters. All the intrusions have the same height (relative to flume bottom), so this window is useful to compare the effects on flume velocity stream lines under different intrusion velocities

Figure 2.11(b) intends to simulate cracks in a sewer system. The inlets has different angles and sizes.

Figure 2.11(c) depict intrusion pipes with the same diameter. Its goal is to analyze the effect of intrusions with the same velocity at different heights.

Figure 2.11(d) shows a diffusion inlet which simulates a crack at 45 degrees. There are two intrusion pipes, one of them is intended to introduce water against the main flow in the pipe.

Figure 2.11(e) consist of 4 pipes with the same diameters distributed through the length and height of the window. However, the intrusion length of these pipes is bigger than the previous windows, it means the effect near the center of the width will be higher..

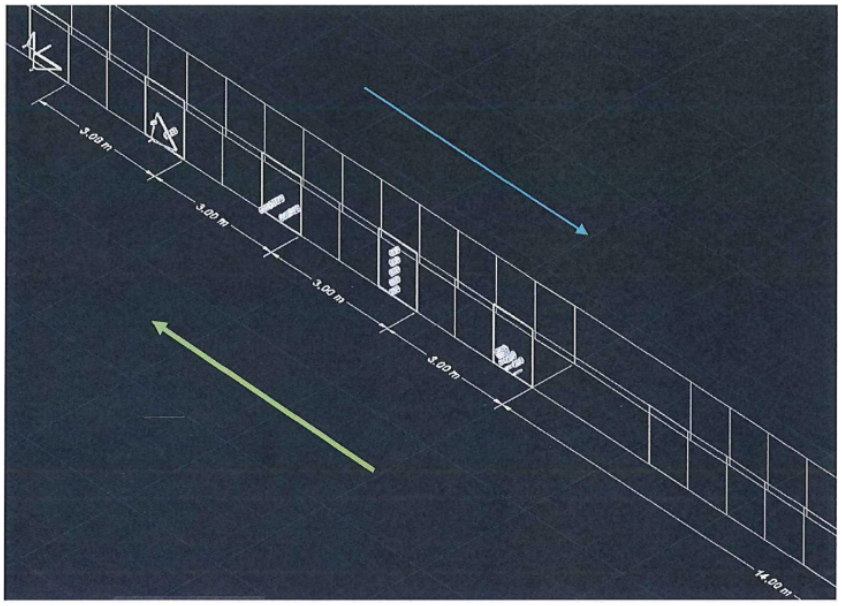

Figure 2.10: Overview of windows disposition in flume (Image taken from [8])

2.1.3. CFD DATA

Computational Fluid Dynamic (CFD) data were necessary to test CFD based methodology results. Since, this data have been obtained by the Navier-Stokes equation solution, the CFD based methodology must converge to similar values. Likewise, several scenarios called data subsampling (Cross section withdrawing test, Sinusoidal movement) were also implemented to simulate the lack of data and test predictability of the proposed methodology.

Cross section withdrawing test: UB flow could be used in such a way the velocity measurement is only done in some cross sections. This procedure requires the set up operates with intermittent movement (translation – rotation - translation). In order to simulate this process in a script different percentages of discretized cross sections (Figure 2.12) were randomly removed from the grid system. In order to fill-in the subsampled grid system, the velocity values in empty volumes have been interpolated with a triangulation from the existing ones.

Sinusoidal Movement: In this measuring process UB flow scans the velocity field while it moves along the flume (continuous translation and rotation), simulated with a sinusoidal function with a certain wavelengths (Figure 3.7(a)). All the data outside that band are removed. A grid is created with the remaining data and all the missing data were replaced with triangulation based interpolation. The sinusoidal functions have different periods to regulate the data remotion.

The CFD data used was obtained by [9] in a experiment to test the capacity of artificial networks to predict velocity distributions. The analyzed system consist on two flumes (A-A and B-B) which intersects each other at 90 degrees. The slope of both flumes is 0. The flow in flume A-A is 3 l/s while the flow in B-B is 1 l/s. Figure 2.14 show two figures of the used CFD data.

The flow in flume A-A is 3 l/s while the flow in B-B is 1 l/s. Figure 2.14 show two figures of the CFD data used.

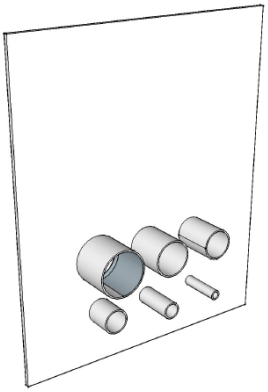

(a) Windows 1: Diameters

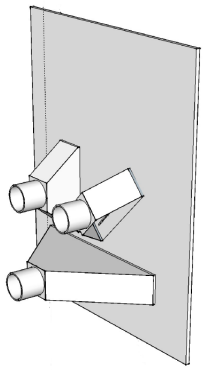

(b) Windows 2: Diffusion

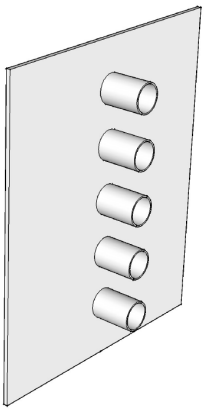

(c) Windows 3: Water levels

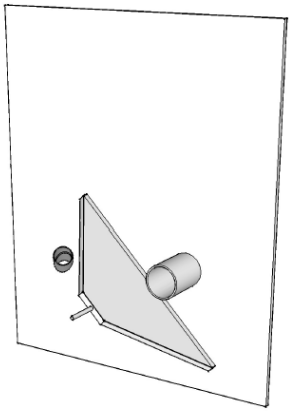

(d) Windows 4: Diffusion-Intrusion

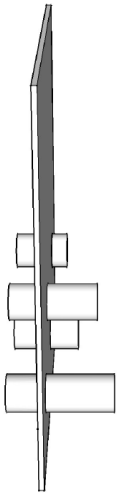

(e) Windows 5: Intrusion

Figure 2.11: Windows used during experiments

2.2. METHODS

According to the right hand convention (Figure 2.7) and with the distance data some position and orientation information of the moving structure is known (z, θ_x (Pitch), and θ_y (Yall)). In order to derive the missed

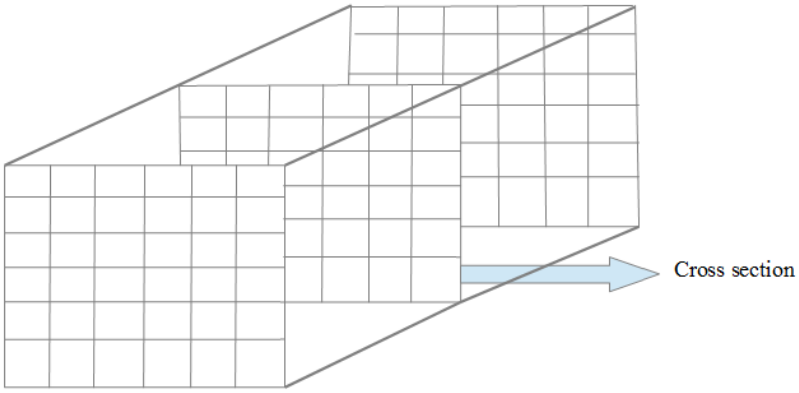

Figure 2.12: Cross sections withdrawing test (Row indicates the removal of a cross section data)

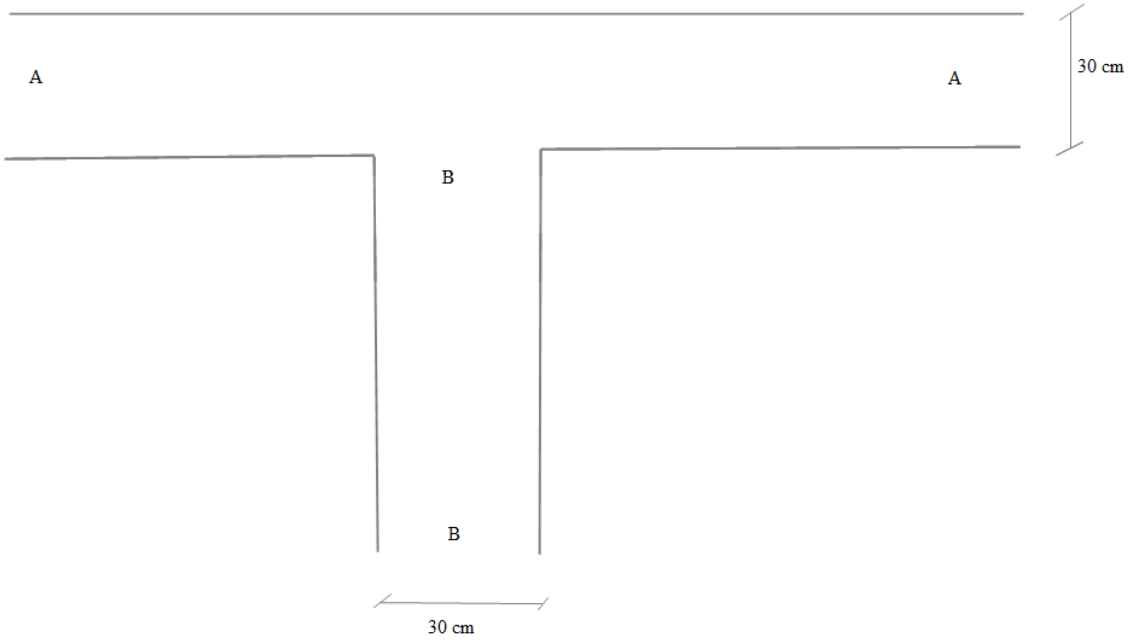

Figure 2.13: CFD system: Top view

information (x, y, and θ_z (Roll)) analysis of video images is needed. There are tiny differences with [6]. θ_z (Roll) has higher values in this study. Small adjustments of the existing code were required. The overall procedure is detailed hereafter.

2.2.1. CAMERA CALIBRATION AND DISTORTION

The back camera as every camera suffers from distortion problems. Distortion affects the image characteristics at its borders, for example a pixel seen by a camera has in reality a certain displacement (Δx, Δy) with respect to the real position. There are two types of distortion: radial and the tangential distortions. Radial distortion (Figure 2.15) are optical peculiarities characterized for representing straight lines as curve lines projections in the lens [10]. The tangential distortion (Figure 2.16) is less important and is caused when the physical elements in lens are not perfectly aligned [11].

In order to know the real positions of the laser dots, the distortion correction need to be applied. Therefore, a non-linear methodology calibration was applied [13].

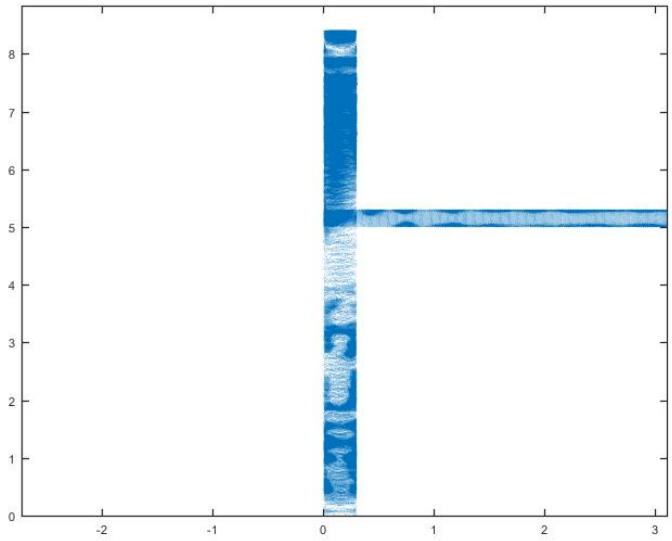

(a) 2D representation of the data

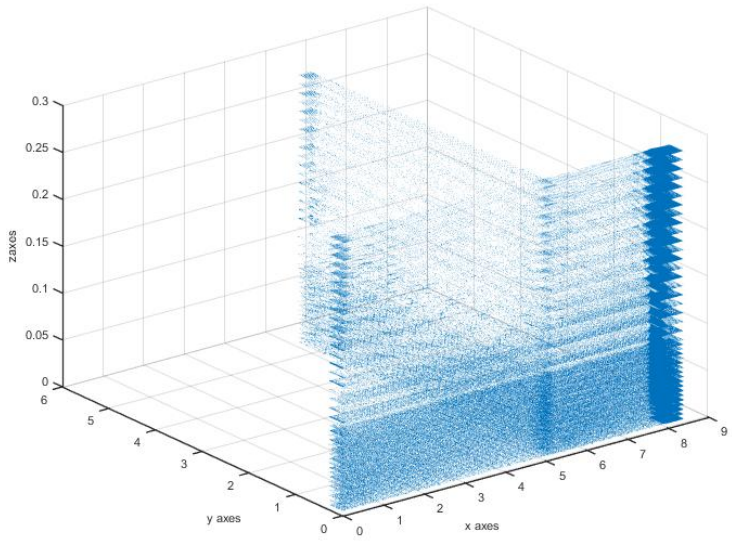

(b) 3D representation of the data

Figure 2.14: CFD data: Velocity vectors

Figure 2.15: Radial distortion (Image taken from [11])

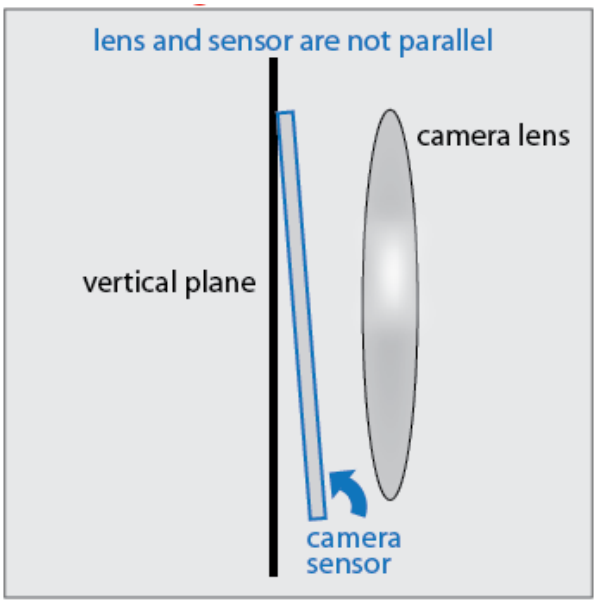

Figure 2.16: Tangential distortion (Image taken from [12])

Table 2.1: Camera calibration mean values

Camera	Len	Aperture	Radial Distortion k1	k2	k3	Tangential Distortion p1	p2	Skew	Mean error in pixels
cam_{back}	Kowa LM4NCM	1.6	-0.0755	0.0991	-0.0630	0.0002	0.0012	-1.4013	0.4438

The calibration methodology to correct radial distortion of the back camera consisted on taking 100 pictures of a checkerboard with different angle rotations (θ_x,θ_y,θ_z). All these images were introduced in Matlab(®) Single Camera Calibration App. This application provides the radial (k_1,k_2,k_3) and tangential distortion coefficients (p_1,p_2) required for this calibration.

The relation between distorted ($x_{distorted}$, $y_{distorted}$) pixel locations and undistorted pixel locations (x, y) are given by Equations 2.2 and 2.3 [13].

$$\begin{aligned} x_{distorted} &= x \cdot \left(1 + k_1 \cdot r^2 + k_2 \cdot r^4 + k_3 \cdot r^6\right) \\ y_{distorted} &= y \cdot \left(1 + k_1 \cdot r^2 + k_2 \cdot r^4 + k_3 \cdot r^6\right) \end{aligned} \tag{2.2}$$

$$\begin{aligned} x_{distorted} &= x + \left[2 \cdot p_1 \cdot y + p_2 \cdot \left(r^2 + 2 \cdot x^2\right)\right] \\ y_{distorted} &= y + \left[p_1 \cdot \left(r^2 + 2 \cdot y^2\right) + 2 \cdot p_2 \cdot x\right] \end{aligned} \tag{2.3}$$

[13] found the distortion parameters (Table 2.1) to correct distortion in back camera when the lens Kowa LM4NCM are used with an aperture is 1.6 (as during the experiment).

2.2.2. POSITIONING OF RAW DATA ALONG THE FLUME

The back camera takes data in a plane (ψ) different than plane of the laser (R3). This difference in planes is because the lasers have a fixed position while the back camera rotates with the set up: a equation to change the reference plane (Equation 2.4) was required [14].

$$Tr = R \cdot T \tag{2.4}$$

R is an orthogonal rotation matrix ($R^{-1} = R^T$)) (Equation 2.6) and T is a translation matrix (Equation 2.5).Tr allows the transformation of a laser plane coordinating to the camera one.

$$T = \begin{pmatrix} 1 & 0 & 0 & X \\ 0 & 1 & 0 & Y \\ 0 & 0 & 1 & Z \\ 0 & 0 & 0 & 1 \end{pmatrix} \tag{2.5}$$

$$R = \begin{pmatrix} R_{11} & R_{12} & R_{13} & 0 \\ R_{21} & R_{22} & R_{23} & 0 \\ R_{31} & R_{32} & R_{33} & 0 \\ 0 & 0 & 0 & 1 \end{pmatrix} \tag{2.6}$$

In Equation 2.6 row 1 is called RIGHT, row 2 is UP, and row 3 is OUT (Figure 2.17). OUT is a normal vector to the PVC plate plane. This vector has as components: R_{31},R_{32}, and R_{33} representing the projection of this vector in the x,y, and z axis. Based on a given plane equation $(ax + by + cz + d = 0)$ a normal vector is defined by $(ai + bj + ck)$ where the coefficients are calculated by Equation 2.7.

$$OUT = \begin{pmatrix} a \\ b \\ c \end{pmatrix} = \begin{pmatrix} R_{31} \\ R_{32} \\ R_{33} \end{pmatrix} = \begin{pmatrix} x1 & y1 & d1 \\ x2 & y2 & d2 \\ x3 & y3 & d3 \end{pmatrix}^{-1}_{R^{(3)}} \begin{pmatrix} 1 \\ 1 \\ 1 \end{pmatrix}_{R^{(3)}} \tag{2.7}$$

Where x_i, y_i represents the fixed position of the lasers on the PVC plate when the laser plane is parallel to the back camera plane. d_i represents the distances measured by the laser in the z position for x_i, y_i .

OUT vector is normalized (Equation 2.8):

$$\begin{pmatrix} R_{31} \\ R_{32} \\ R_{33} \end{pmatrix} = \frac{\begin{pmatrix} R_{31} \\ R_{32} \\ R_{33} \end{pmatrix}}{|OUT|} \tag{2.8}$$

A change of nomenclature is necessary to indicate that OUT is unitary (Equation 2.9):

$$OUT = R_{31}i + R_{32}j + R_{33}k = n_{n1}i + n_{n2}j + n_{n3}k \tag{2.9}$$

UP vector (R_{21},R_{22},R_{23}) is calculated by Equation 2.10 [14].

$$UP = R_{21}i + R_{22}j + R_{23}k = UP_w - (UP_w \cdot OUT) \times OUT \tag{2.10}$$

Where:

$$UP_w = \begin{pmatrix} 0 & 1 & 0 \end{pmatrix} \tag{2.11}$$

Likewise OUT, UP is also normalized and changing the nomenclature (Equation 2.12)

$$UP = R_{21}i + R_{22}j + R_{23}k = o_{n1}i + o_{n2}j + o_{n3} \tag{2.12}$$

RIGHT is a vector normal to both UP and OUT obviously calculated from the vectorial product

$$RIGHT = R_{11}i + R_{12}j + R_{13}k = UP \times OUT \tag{2.13}$$

Equation 2.13 provides unit vector because OUT and UP are normalized vectors. Equation 2.14 is needed to modify nomenclature:

$$RIGHT = R_{11}i + R_{12}j + R_{13}k = r_{n1}i + r_{n2}j + r_{n3}k \tag{2.14}$$

Rotation matrix is given by Equation 2.15:

$$R = \begin{pmatrix} r_{n1} & r_{n2} & r_{n3} \\ o_{n1} & o_{n2} & o_{n3} \\ n_{n1} & n_{n2} & n_{n3} \end{pmatrix} \tag{2.15}$$

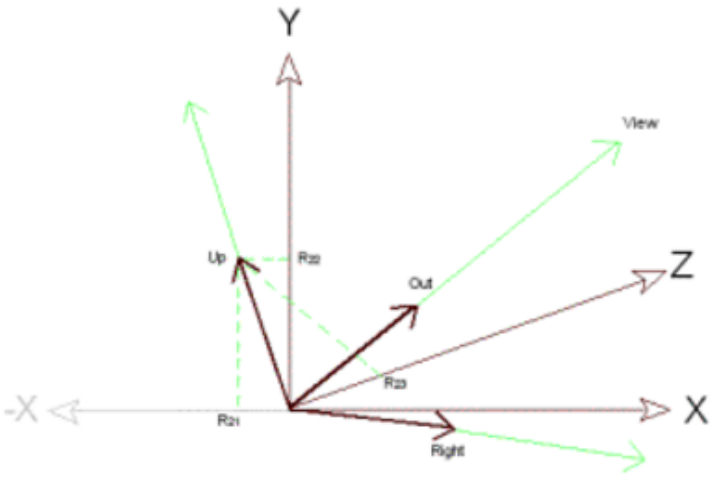

Figure 2.17: Scheme for rotation matrix (Image taken from [14])

ROTATION CALCULATION

Equation 2.4 is used to change the coordinates of a point according to the camera plain. Hence, this equation can be re written as:

$$Tr = pc_{back} = R \cdot T = R \cdot p_{R_3} \tag{2.16}$$

pc_{back} are points in the back camera plane.

p_{R3} represent the point pc_{back} but with respect to the lasers plane

From the experiments back camera points pc_{back} are obtained, the goal is to obtain those points with respect to laser plane (p_{R3}). Equation 2.19 is an adjustment of Equation 2.16 for this goal. However, back camera data needs to be adjusted due to its distance to the PVC plate. A scaling factor (s_{back}) is used as seen in Equation 2.19. Because back camera only see two dimensions, the equation is also reduced:

$$p_{R2} = s_{back} \cdot R^T \cdot pc_{back} \tag{2.17}$$

The PVC plate moves while the lasers has a fixed position. Consequently, there is translation (x,y,z) and deformation (θ_z) of the laser points in the PVC plate plane which needs corrections. Figure 2.18 depicts the reference triangle formed by the three lasers at the start of the test (Laser plane parallel to back camera plane). z coordinate is corrected with $1/c$ (c is the third component of OUT). In order to correct x, y a translation of coordinates is necessary to bring the origin of the triangle modified to the origin of the original triangle (Figure 2.18).

$$p_{R_{i=1,2,3}} = p_{R_{i=1,2,3}} - p_{R_1} \tag{2.18}$$

Where the suffix i=1,2,3 refers to the laser 1, 2, and 3 points respectively.

Where p_{R_1} (Equation 2.19) is a translation vector:

$$p_{R_1} = \begin{pmatrix} X_\Delta \\ Y_\Delta \end{pmatrix} \tag{2.19}$$

Figure 2.19 illustrates graphically the coordinate translation step.

θ_z is found (Equation 2.20) when two concurrent sides of the modified triangle and reference triangle are transformed to vectors (Figure 2.20) .

$$A \cdot B = |A||B| \cdot \cos(\theta_z) \tag{2.20}$$

θ_z needs to be modified by a sign function to take into account the direction of the angle (Positive in a counter wise direction). The x coordinates for the modified triangle are subtracted from the reference triangle.

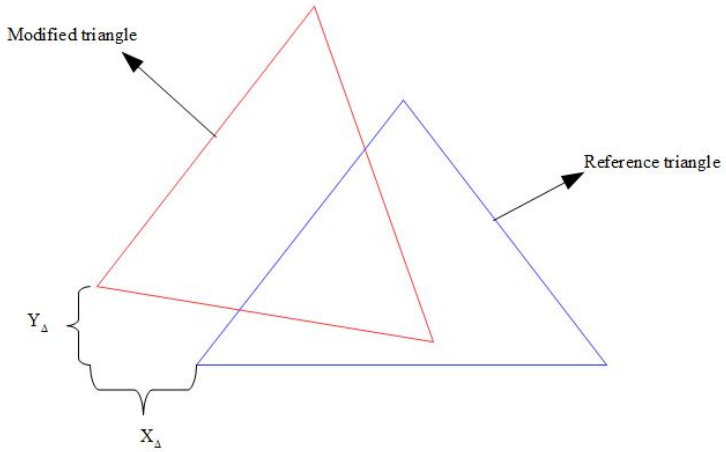

Figure 2.18: Original triangle-Modified triangle translation

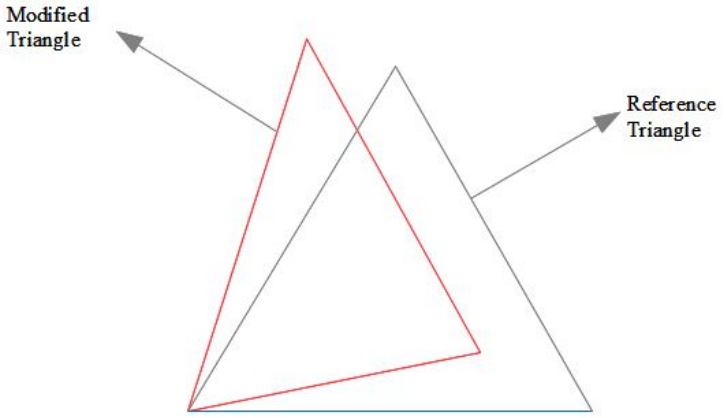

Figure 2.19: Translation result of the Triangle Modified

$$\cos(\theta_z) = \frac{sign(A \cdot B)}{|A||B|} \tag{2.21}$$

[6] provides the equations for θ_x and θ_y. In the following formulas a,b , and c are components of OUT vector.

$$\cos(\theta_x) = \frac{\sqrt{a^2 + c^2}}{\sqrt{a^2 + b^2 + c^2}} \tag{2.22}$$

$$\cos(\theta_y) = \frac{c}{\sqrt{a^2 + c^2}} \tag{2.23}$$

Consequently, at the end of these step θ_z, θ_x ,θ_y are found. These angles are used to rotate the UB flow velocity points to create a raw velocity cloud. The procedure is explained in the Subsection 2.2.3.

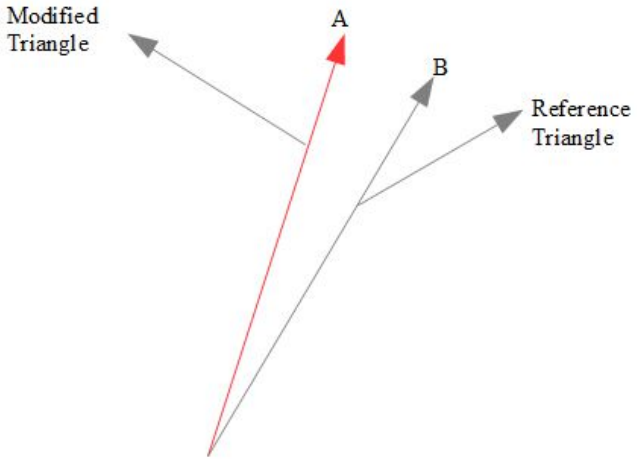

Figure 2.20: Two points selected from the Modified Triangle and the Reference triangle

2.2.3. CREATION OF THE RAW VELOCITY CLOUD

Once angles θ_x, θ_y and θ_z have been found, the position of the velocities taken by the UB flow can be obtained. Velocity data is taken at different depths with respect to the longitudinal axes of the device (z). In order to know the measured points positions first it is going to be analyzed the case where there is no rotation, and later the case including rotation.

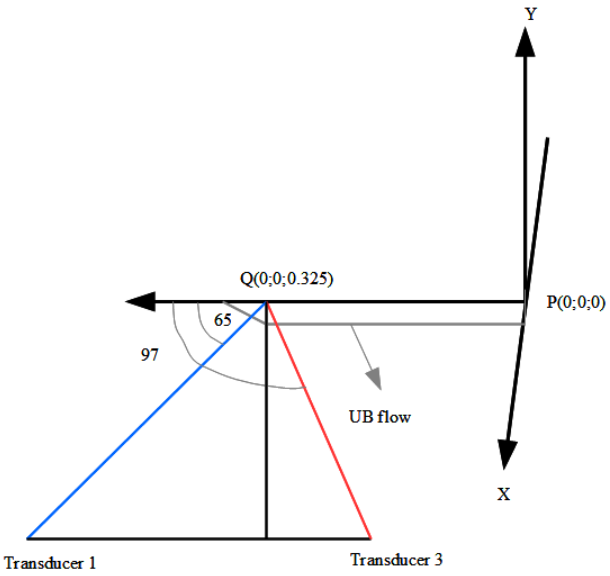

Figure 2.21: Scheme of UB Flow data acquisition

VELOCITY LOCATION WITHOUT ROTATION

Figure 2.21 shows a scheme of the way UB flow data is taken. P represents a relative origin of the UB flow which is directly below the PVC plate (See Figure 2.3). Point Q represents the UB flow transducer origin. The UB flow provides the **velocity component which follows the beam direction**. For Transducer 1 the scheme presented in Figure 2.22 is used to explain the velocity point location.

Figure 2.22 depicts that the position of P'(P'_x, P'_y, P'_z) with respect to P is given by the Equations 2.24 2.25 and 2.26.

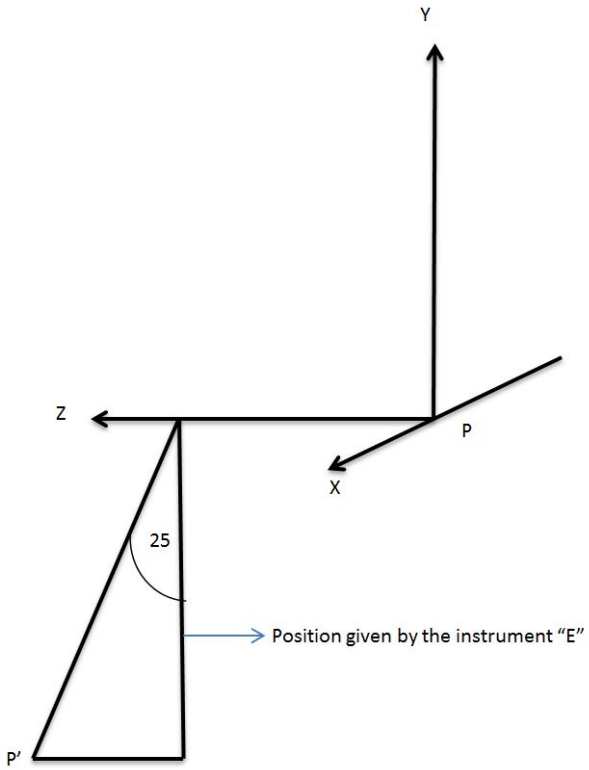

Figure 2.22: Scheme for velocity position on beam 1

$$P'z = \tan(25) \cdot E + 0.325 \tag{2.24}$$

$$P'x = 0 \tag{2.25}$$

$$P'y = -E \tag{2.26}$$

The scheme for transducer 3 represented by the point P" (P''_x, P''_y, P''_z) is shown in Figure 2.23.The transducer velocity position equations is represented by Equation 2.27, 2.28, and 2.29.

$$P''z = \tan(-7) \cdot E + 0.325 \tag{2.27}$$

$$P''x = 0 \tag{2.28}$$

$$P''y = -E \tag{2.29}$$

VELOCITIES LOCATION INCLUDING ROTATION

P' and P" (Figures 2.22 and 2.23) must be rotated around the three axes as well as to do a coordinate translation to have the data in a common reference system (laser plane). [15] provides the information how to rotate two coordinates while the remaining coordinate stays constant as well as how to do the translation of coordinates.

Rotation around x axis: The rotation around the x axis (Considered positive in counter clock direction) is calculated with Equation 2.30 and 2.31.

$$PP' = PP \cdot Rx \tag{2.30}$$

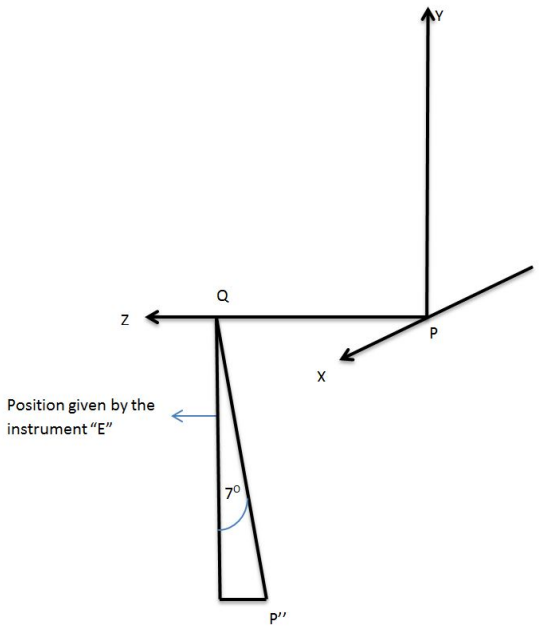

Figure 2.23: Scheme for velocity position on beam 3

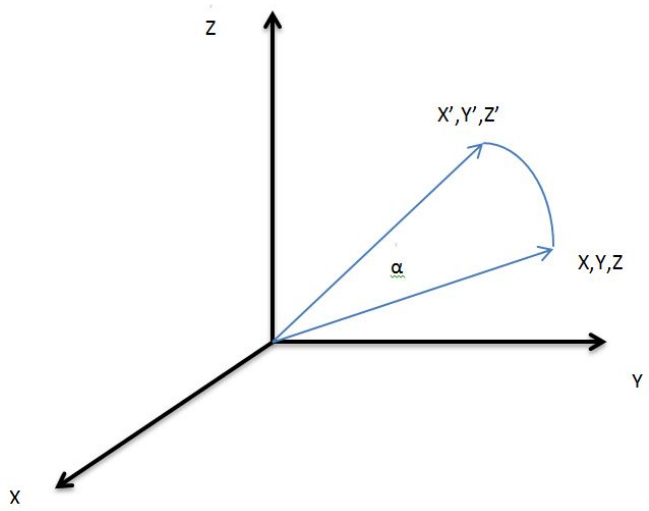

Figure 2.24: Rotation around x axis

$$PP' = \begin{pmatrix} x & y & z & 1 \end{pmatrix} \cdot \begin{pmatrix} 1 & 0 & 0 & 0 \\ 0 & \cos(\alpha) & \sin(\alpha) & 0 \\ 0 & -\sin(\alpha) & \cos(\alpha) & 0 \\ 0 & 0 & 0 & 1 \end{pmatrix} \tag{2.31}$$

Rotation around y axis: Rotation around *y* axis (Figure 2.25) is represented by Equations 2.34 and 2.33.

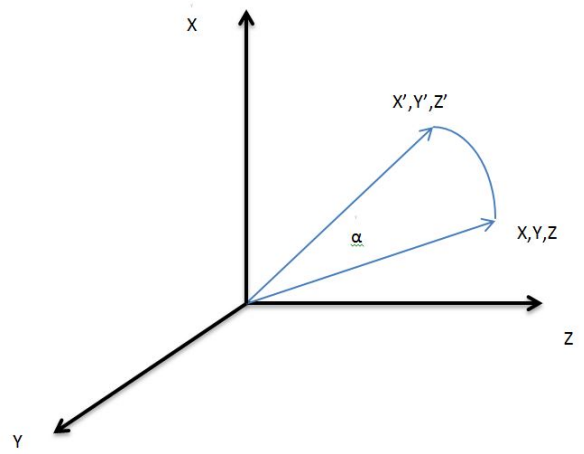

Figure 2.25: Rotation around y axis

$$PP' = PP \cdot Ry \tag{2.32}$$

$$PP' = \begin{pmatrix} x & y & z & 1 \end{pmatrix} \cdot \begin{pmatrix} \cos(\alpha) & 0 & -\sin(\alpha) & 0 \\ 0 & 1 & 0 & 0 \\ \sin(\alpha) & 0 & \cos(\alpha) & 0 \\ 0 & 0 & 0 & 1 \end{pmatrix} \tag{2.33}$$

Rotation around z axis: Equations 2.34 and 2.35 indicates the calculation of rotation around *z* axis (Figure 2.26).

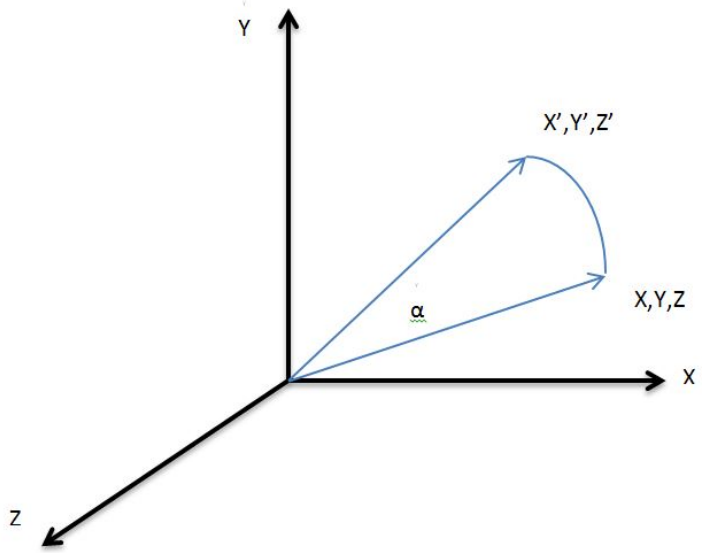

Figure 2.26: Rotation around z axis

$$PP' = PP \cdot Rz \tag{2.34}$$

$$PP' = \begin{pmatrix} x & y & z & 1 \end{pmatrix} \cdot \begin{pmatrix} \cos(\alpha) & \sin(\alpha) & 0 & 0 \\ -\sin(\alpha) & \cos(\alpha) & 0 & 0 \\ 0 & 0 & 1 & 0 \\ 0 & 0 & 0 & 1 \end{pmatrix} \tag{2.35}$$

Translation of coordinates: In order to translate a certain point PP(x,y,z) to a new origin (tx,ty,tz), a translation matrix is necessary. The translation of a point is given by Equation 2.36.

$$PP' = PP \cdot T \tag{2.36}$$

$$PP' = \begin{pmatrix} x & y & z & 1 \end{pmatrix} \cdot \begin{pmatrix} 1 & 0 & 0 & 0 \\ 0 & 1 & 0 & 0 \\ 0 & 0 & 1 & 0 \\ tx & ty & tz & 1 \end{pmatrix} \tag{2.37}$$

Figure 2.27 portrays the rotation of P' around the axes x, y, and z. Besides, a translation of coordinates is necessary to have the final position with respect to O (Figure 2.27). The translated and rotated point P'' is found with Equation 2.38.

$$P'' = P' \cdot Rz \cdot Rx \cdot Ry \cdot T \tag{2.38}$$

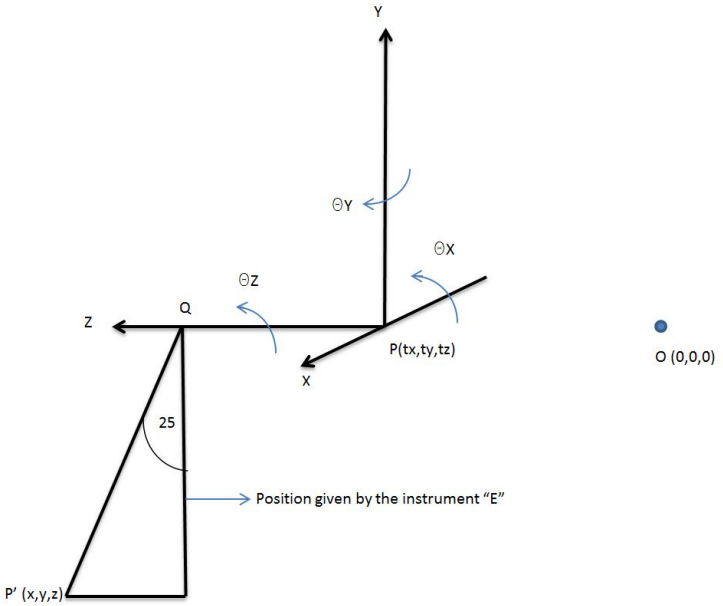

Figure 2.27: Scheme for rotation and translation of a velocity point

VELOCITIES PROJECTION

UB flow can provide 1-D data (U_z) when velocity measurement from transducer 1 and 3 are analyzed separately. When the analysis are combined together, a 2-D velocity data can be extracted:U_z,U_y in the UB Flow reference system. This procedure requires velocities of both transducer in the same volume, which is impossible due to i) the translation and rotation movement of the UB Flow (no measurement is done at the same time and at the same place) and ii) the different transducer configurations. Consequently, interpolation procedures needs to be implemented in order to get V1 and V3 in each volumes of the grid. 3-D velocity data are then derived from the UB flow orientation: θ_z is used to project the rotated vertical component (in the

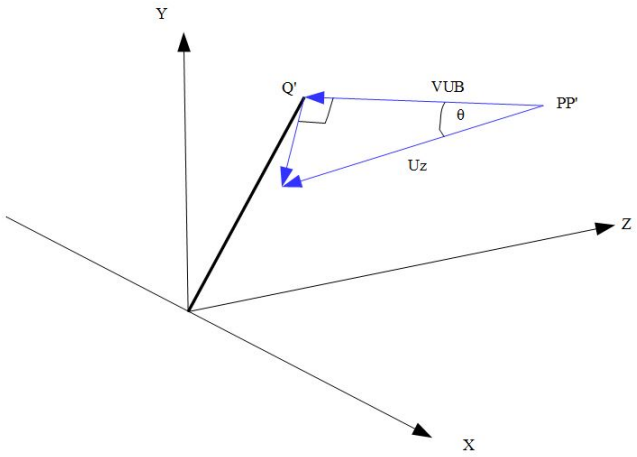

Figure 2.28: Projection of velocities

UB Flow reference system) of the velocity and get U_y and U_x . The formulation for 1-D velocities is presented below.

UB flow velocities follows the transducer direction, but the required velocity (U_z) is one with its components following the required coordinate system (Figure 2.7) therefore projections are required. UB flow velocity must be projected in the direction z "U_z ". Points Q' and PP' are the result of applying Equation 2.38 on Q and P' of Figure 2.27. Q'(d,e,f) and PP'(g,h,i) forms a vector $\overrightarrow{PP'-Q'} = (g-d, h-e, i-d) = (j,k,l)$. Vector PP'-Q' is transform into unitary through the division of each component by its modulus ($\sqrt{j^2+k^2+l^2}$). The angle formed by $\overrightarrow{PP'-Q'}$ and the direction z (0,0,1) is θ (Equation 2.39).

$$\vec{z} \cdot \overrightarrow{PP'-Q'} = \left|\vec{z}\right| \left|\overrightarrow{PP'Q'}\right| \cos(\theta) \tag{2.39}$$

The z component of the velocity in the desired coordinate system (U_z) is obtain through a trigonometric relation with the velocity measured by the UB flow (V_{UB}) (Equation 2.40)

$$U_z = \frac{V_{UB}}{\cos(\theta)} \tag{2.40}$$

An additional observation is that the set-up was moving during the experiments, so the velocity detected by the transducer is the velocity of the water plus the velocity of the set-up:

$$U_z = U_z - V_{setup} \tag{2.41}$$

Velocity calculated with Equation 2.41 provide us with water velocity only. V_{set-up} is obtained by combining laser data and its time stamp.

2.2.4. RAW DATA PROCESSING

In this section, the steps to get 3-D velocities components from the UB flow are explained:

Nyquist correction When an ultrasonic wave sent by the UB flow find an acoustic scattered, this change its wave frequency (Doppler shift). Ub flow measurement in a cell is based on n pulses (ultrasonic waves). This way of measurement is valid in a certain velocity range. The ultrasonic wave period determines the measurement depth and intervals when UB flow measures the Doppler shift. When the interval between two pulses is too long, the measurement of the Doppler shift suffers a phase jump leading to incorrect velocity values calculation. According to [7], from a frequency point of view this phase jump is comparable to exceed the limit given by Nyquist-Shannon theorem. In order to correct this phenomena from the raw data Equation 2.42 is applied when raw velocities values go outside the UB flow configuration.

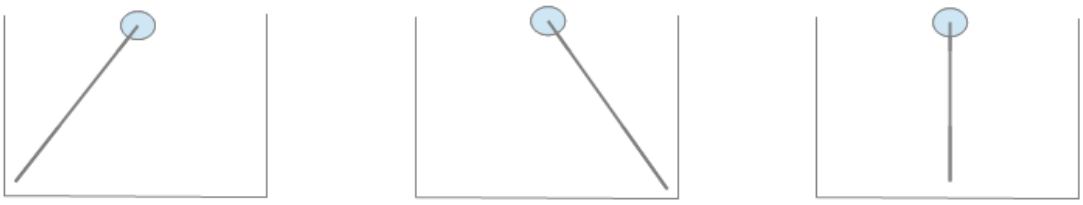

Figure 2.29: UB flow rotation during experiment

According to our adjustment, Transducer1 velocities must be comprised between -0.05 m/s and 0.278 m/s, while for transducer 3 the range is -0.02 m/s to 0.125 m/s.

$$V_{UB} = V_{UBraw} - \frac{cs \cdot PRF}{2fo} \tag{2.42}$$

Where:

V_{UB}*:* Raw UB flow velocity corrected (m/s)

V_{UBraw}*:* Raw velocity measured by the UB flow (m/s)

c_s is the sound speed which value is around 1480 m/s

fo: emission frequency (Hertz)

PRF: Repetition frequency (Hertz)

Rotation As previously described, and with UB flow geometry, measurement beams can be placed on the flume reference system through the application of rotation/translation matrices .

Grid system creation The velocities points of the reach has been divided in regular volumes.

Interpolation Due to the translation and rotation speed, significant part of the volumes does not have data: an interpolation methodology is required. A first attempt was done with a "nearest neighbor"interpolation, but due to the triangulation done for this methodology data is going to increase from the walls until reach the beam data (Figure 2.29). It makes sense only when the beam is was located in the middle of the flume. Hence, this interpolated data may need a further correction with another methodology. At the end of these step, there are V_1 and V_3 velocity data at each volume (V_1 and V_3 are UB flow velocities from Transducer 1 and 3).

3-D velocities In order to obtain the velocity components in the reference system (U(U_x,U_y,U_z)) a two step projection is required.

$U_z = 1.873 \cdot V_{TR1} - 1.71 \cdot V_{TR3}$

$Vy_{UB} = -0.23 V_{TR1} - 0.7975 \cdot V_{TR3}$

Where:

U_z Component of the flow velocity in z direction (m/s)

V_{TR1} Velocity from transducer 1 (m/s)

V_{TR3} Velocity from transducer 3 (m/s)

Vy_{UB} Rotated vertical velocity measured by the UB flow, it need to be projected to follow the reference system (Figure 2.30). To do the projection it is used the following formulas:

$U_y = V_{yUB} \cdot \cos(\theta_z)$

$U_x = V_{yUB} \cdot \sin(\theta_z)$

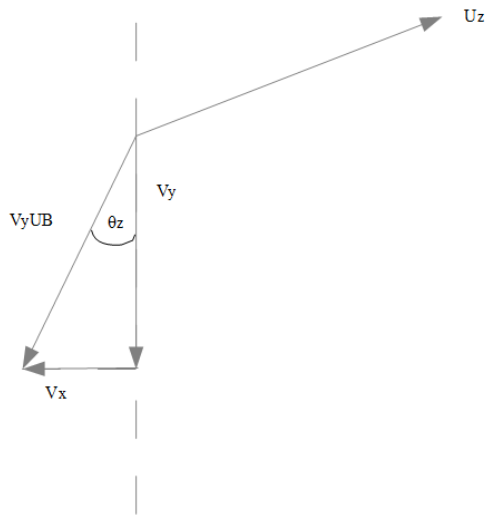

Figure 2.30: Velocity components projection scheme

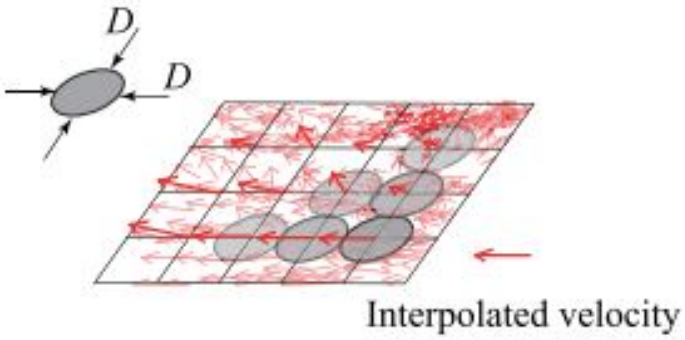

Figure 2.31: Isotropic gridding (Image taken from [16])

2.2.5. INTERPOLATION METHODOLOGY BASED ON CFD METHODOLOGY

Due to the lack of hydraulic meaning of the previously used "nearest neighbor"interpolation , existing data (U_x,U_y,U_z) require to be corrected by an hydraulic approach.

[16] propose an interpolation methodology based on Fractional Step Method for solving CFD problems. This new methodology has shown superior performance over Inverse Density Point (IDP) and Krigging when the density point has a value of 3, according to [16]. The density point is the ratio between number of velocity data and grid number.

The steps for this methodology are explained in the following paragraphs:

1. *Preprocessing of raw data* is used to eliminate random errors and artifacts. This process in the current work was replace by Nyquist correction.

2. *Isotropic griding* was intended to find the preference velocity direction. At each node the angle α (Equation 2.43) was found. In order to calculate this angle, a mean U_x and U_y within a circle with diameter D and origin (x_o,y_o) were calculated.

$$\alpha = \frac{\overline{U_x}}{\overline{U_y}} \tag{2.43}$$

In order to know if a certain point is inside a circle, the following inequality must be met:

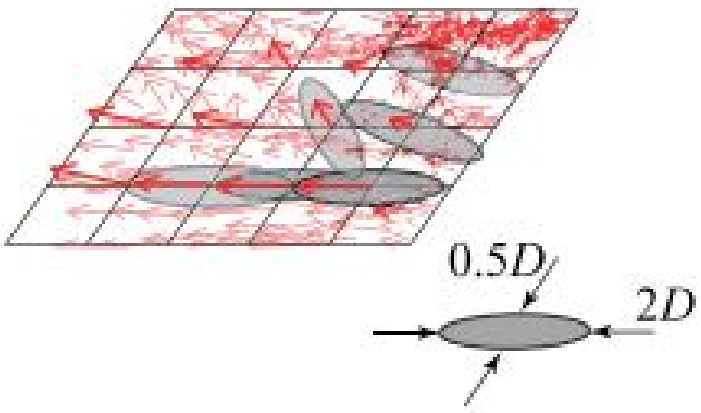

Figure 2.32: Anisotripoic gridding (Image taken from [16])

$$(x-xo)^2+(y-yo)^2 \leq \left(\frac{D}{2}\right)^2 \tag{2.44}$$

3. *Anisotropic griding* calculates velocities average inside an ellipse. This ellipse has a rotation angle obtained in the isotropic griding (Figure 2.32). A point inside an ellipse with an angle α and center (xo,yo) meets the inequality shown in Equation 2.45.

$$\frac{((x-xo)\cdot\cos(\alpha)-(z-zo)\cdot sin(\alpha))^2}{a2^2}+\frac{((x-xo)\cdot\sin(\alpha)+(z-zo)\cdot cos(\alpha))^2}{b2^2}\leq 1 \tag{2.45}$$

a2 is the minor axis and b2 is the major axis.

FORMULATION

The interpolation method to be tested is based on a Computational Fluid Dynamics (CFD) solution procedure. A solution scheme applicable for all CFD problems is presented by [17] (Figure 2.33). Hereafter, the basic concept implied by this method are briefly explained.

PHYSICAL DOMAIN AND PHYSICAL PHENOMENA

The physical domain is the Scheldt flume in Deltares. The physical phenomena is the fluid motion characteristics in a flume with intrusions.

GOVERNING EQUATIONS

Navier Stokes equations

The Navier Stokes equations are based on the conservation principle: "For an isolated system certain physical measurable quantities are conserved over a local region "[17]. This conservation principle is valid from a Lagrangian description. In this description, the domain is sub dived into volumes and each one is followed as it moves in space and time (Material Volume). On the other hand, an Eulerian description analyze the flow properties at a fixed point in the domain "Control Volume ". The last description is preferable due to a higher applicability to analyze fluid flow problems. The Reynolds transport theorem is used to relate Eulerian and Lagrangian descriptions [17] (Equation 2.46).

$$\left(\frac{dB_f}{dt}\right)_{MV}=\frac{d}{dt}\left(\int\int\int_{V(t)} b_f\cdot\rho\cdot dB\right)+\left(\int\int_{S(t)} b_f\cdot\rho\cdot Vr\cdot n\cdot ds\right) \tag{2.46}$$

Where:

Bf is the fluid property

bf is the intensive value (Amount of B per unit mass)

Vr is a reference velocity, if the volume control is moving then this value is equal to fluid velocity minus control volume velocity (m/s)

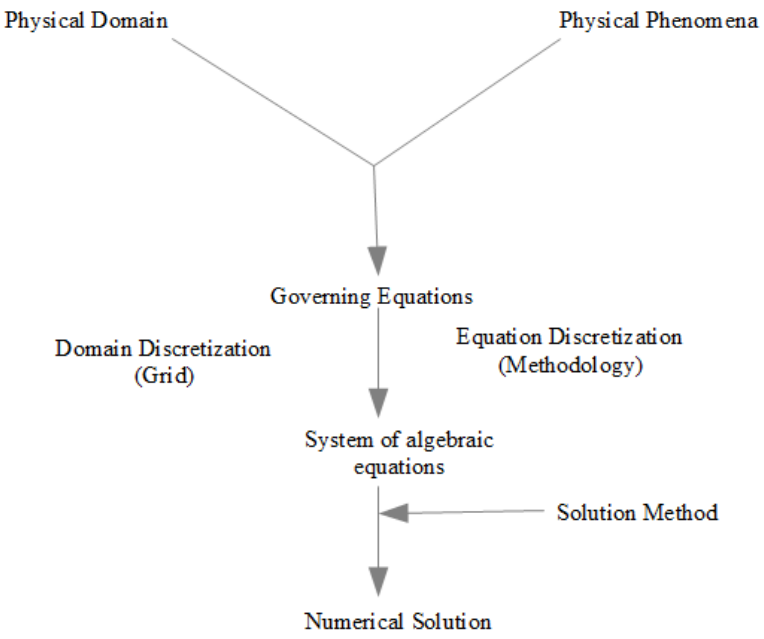

Figure 2.33: CFD solution scheme (Imagen taken from [17])

V control volume (L^3)
S surface of control surface (L^2)
ρ water density (M/L^3)
Equation 2.46 states that the instantaneous change of B in the material volume is equal to the instantaneous change of B in the control volume plus the net flux of B in the surface of the control volume.

Momentum Equation

The momentum conservation states that in a material volume the time rate change of the momentum is equal to the sum of forces acting on it [17] [18].

The forces acting over the material volume are divided into two groups: Surface forces and Body forces.

Surface Forces: The surface forces acting on the material volume are due to pressure and viscous stresses. In the current formulation to obtain the viscous forces a Newtonian fluid is supposed. In a Newtonian fluid there is a linear relation between the shear stress and shear rate:

$$\tau = \mu \cdot \frac{dU_x}{dy} \tag{2.47}$$

Where:
τ is the shear stress (Pascals)
μ dynamic viscosity ($Pa \cdot s$)
$\frac{du}{dy}$ change of velocity over the distance ($\frac{1}{s}$)
Body forces: To this category correspond forces due to gravitational fields and rotation.
The final equation in a Eulerian description is depicted in Equation 2.48.

$$U_t = -U \cdot \nabla U + \nu \cdot \nabla^2 U - \frac{\nabla P}{\rho} \tag{2.48}$$

Where:

U_t Local acceleration ($\frac{m}{s^2}$)

$U \cdot \nabla U$ Convective acceleration ($\frac{m}{s^2}$)

$\nu \cdot \nabla^2 U$ Viscous forces ($\frac{m}{s^2}$)

$\frac{\nabla p}{\rho}$ Pressure forces ($\frac{m}{s^2}$)

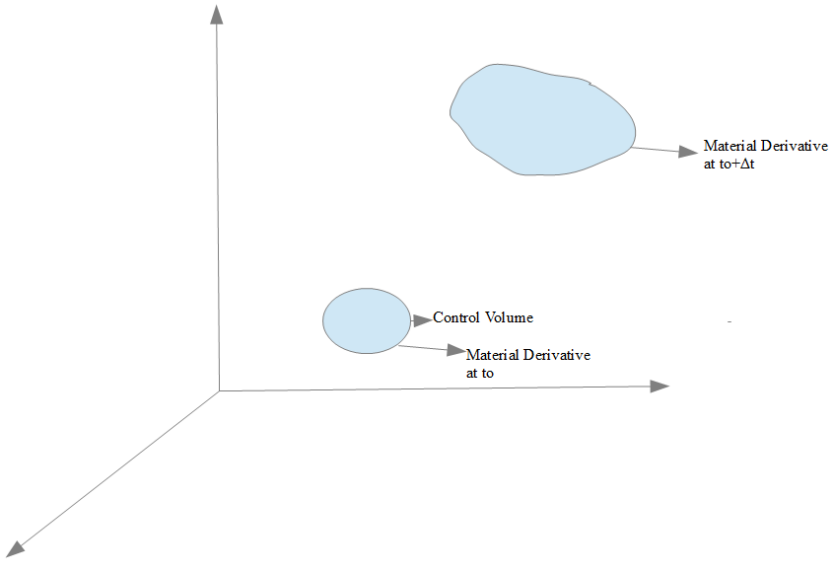

Figure 2.34: Eulerian Description-Lagrangian Description

Mass Balance

This conservation law states that there is no mass change in the material derivative [17]. The resulting equation at Eulerian description is:

$$\frac{\partial \rho}{\partial t} + \nabla \cdot \rho U = 0 \tag{2.49}$$

The incompressibility principle means ρ does not change over time and space. Equation 2.50 shows the final result for the mass balance equation.

$$\nabla U = 0 \tag{2.50}$$

$$\nabla = \left(\frac{\partial}{\partial x}, \frac{\partial}{\partial y}, \frac{\partial}{\partial z} \right) \tag{2.51}$$

$$U = \left(U_x, U_y, U_z \right) \tag{2.52}$$

$$\nabla^2 = \left(\frac{\partial^2}{\partial x^2}, \frac{\partial^2}{\partial y^2}, \frac{\partial^2}{\partial z^2} \right) \tag{2.53}$$

DOMAIN DISCRETIZATION

The domain is divided into pieces in the three direction forming a grid system. Figure 2.35(a) shows an example of a non-staggered grid in which velocities and pressures are stored at the node point. This grid scheme has the downside of having problems with the pressure-velocity coupling as well as pressure oscillation [19]. On the other hand; in a staggered grid (Figure 2.35(b)) the grid system consist on cells. In the center of the cells pressures are stored while in its surrounding the components of velocity are stored. For this grid system decoupling does not occur but its implementation is more complicated.

FRACTIONAL STEP METHOD

In order to solve the Navier-Stokes equations, several methodologies have been developed. The Fractional Step Method is one of them. The Fractional Step Methodology is consider nowadays as a primitive formulation based on a pressure correction approach [20].In order to get the formulation of this methodology the Navier Stokes equations are presented again:

Momentum Equation (Equation 2.48)

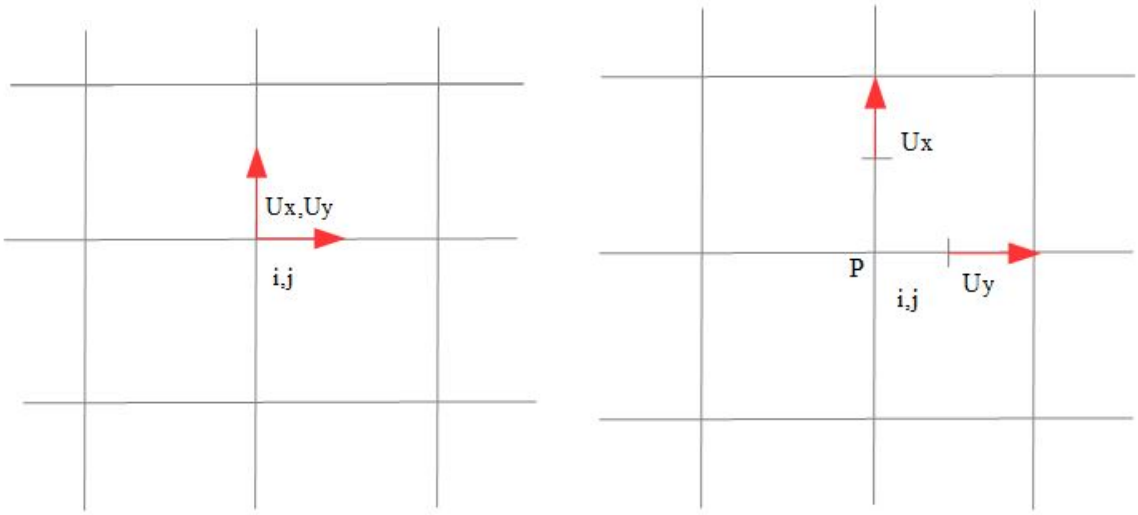

(a) Non-staggered (b) Staggered

Figure 2.35: Staggered and non-staggered grid variables arrangement

$$U^t = -U \cdot \nabla U + \nu \cdot \nabla^2 U - \frac{\nabla P}{\rho}$$

Mass balance equation (Equation 2.50)

$$\nabla U = 0$$

In Fractional step method, the momentum equation is solved without the pressure term (Equation 2.54), to get an initial velocity field (U^t)

$$U^t = U^n + (-A_D^n + D_D^n) \tag{2.54}$$

In Equation 2.54 A_D represents the discretization of convective acceleration while D_D represents the discretization of the viscous forces term.

U^t is projected into the incompressible filed with the pressure term (Equation 2.55)

$$U^{n+1} = U^t - \frac{\Delta t \cdot \nabla P^{n+1}}{\rho} \tag{2.55}$$

According to [21], pressure is obtained by applying divergence (∇) and enforcing incompressibility to momentum equation ([19] justify to take the divergence due to the form of the continuity equation) plus continuity equation to force incompressibility. According to [18], divergence is the tendency of a field to radiate outward a surface.

$$\frac{U^{n+1} - U^n}{\Delta t} = -\frac{\nabla P^{n+1}}{\rho} \tag{2.56}$$

$$U^{n+1} = U^n - \frac{\Delta t}{\rho} \cdot \nabla P^{n+1} \tag{2.57}$$

$$\nabla \cdot \left(U^{n+1}\right) = \nabla \cdot \left(U^n - \frac{\Delta t}{\rho} \cdot \nabla P^{n+1}\right) \tag{2.58}$$

$$\nabla U^{n+1} = 0 \tag{2.59}$$

$$\nabla^2 P^{n+1} = \frac{\rho}{\Delta t} \nabla \cdot U^n \tag{2.60}$$

Equation 2.60 is called Poisson equation. Rearranging equations to get a logic order, this methodology has the following steps:

1) Solution of Navier-Stokes equation without pressure (Equation 2.54)

2) Calculation of the pressure distribution through the solution of the Poisson equation (Equation 2.60).

3) Velocities are corrected using the pressure distribution calculated (Equation 2.55).

An important aspect to consider for the use of this methodology to the current thesis work is the availability of velocity data. Indeed, the first step is not necessary because the measured data is the velocity approximation U^t and is at the same time U^n (Equation 2.55 change to Equation 2.61). Then, this velocity is used to calculate Poisson equation and pressure distributions. This Pressures are used to calculate the correction of the velocities. The corrected velocities are used as initial value to solve the Poisson equation again. There is a new correction of velocities based on the pressures obtain with Poisson Equation. This loop is done until there is convergence of the velocity values.

$$U^{n+1} = U^n - \frac{\Delta t \cdot \nabla P^{n+1}}{\rho} \tag{2.61}$$

A Finite Difference Method is used to solved the differential equation system. This methodology is based on replacing the differential equations at each grid point by an approximation in term of the values at the grid nodes [19]. Each grid point generates an equation representing the integration of the differential equation at that point. This process is called a **Local Assembly** of the mesh. The construction of a system taking into account the individual contribution of each node is called **Global assembly**. This system has a form $A[T] = b$. In this system **A** represents the coefficients of the pressure, **T** are the pressures which are unknown, and **b** is the independent vector which is a function of the velocities.

EQUATION DISCRETIZATION NON-STAGGERED CASE

Approximation to the first derivative

Equation 2.55 contains the first derivative of the pressure. Taylor expansion (Equation 2.62) is used to get an analytical expression for this derivative (Equation 2.63).

$$\phi(x) = \phi(x_i) + (x - x_i)\left(\frac{\partial \phi}{\partial x}\right)_i + \frac{(x-x_i)^2}{2!}\left(\frac{\partial^2 \phi}{\partial x^2}\right)_i + \frac{(x-x_i)^3}{3!}\left(\frac{\partial^3 \phi}{\partial x^3}\right)_i + \cdots + \frac{(x-x_i)^n}{n!}\left(\frac{\partial^n \phi}{\partial x^n}\right) \tag{2.62}$$

Based on Equation 2.62, it is possible to get an equation for the first derivative:

$$\left(\frac{\partial \phi}{\partial x}\right)_i = \frac{\phi(x) - \phi(x_i)}{x - x_i} - \frac{x - x_i}{2}\left(\frac{\partial^2 \phi}{\partial x^2}\right)_i + HOT \tag{2.63}$$

HOT (High Order Terms) can be neglected if the distance between grid points is small. In order to approximate first derivative there are two options: a forward approximation (Equation 2.63 analyzed in x_{i+1} resulting in Equation 2.64) or a backward approximation (Equation 2.63 analyzed in x_{i-1} resulting in Equation 2.65).

$$\left(\frac{\partial \phi}{\partial x}\right)_i = \frac{\phi(x_{i+1}) - \phi(x_i)}{x_{i+1} - x_i} \tag{2.64}$$

$$\left(\frac{\partial \phi}{\partial x}\right)_i = \frac{\phi(x_{i-1}) - \phi(x_i)}{x_{i-1} - x_i} \tag{2.65}$$

A centered approximation is obtained (Equation 2.66) by subtracting the forward approximation from the backward approximation.

$$\phi(x_{i+1}) = \phi(x_i) + (x_{i+1} - x_i)\left(\frac{\partial \phi}{\partial x}\right)_i$$

$$\phi(x_{i-1}) = \phi(x_i) + (x_{i-1} - x_i)\left(\frac{\partial \phi}{\partial x}\right)_i$$

$$\left(\frac{\delta \phi}{\delta x}\right)_i = \frac{\phi(x_{i+1}) - \phi(x_{i-1})}{x_{i+1} - x_{i-1}} \tag{2.66}$$

There are two additional approximations to be found: An approximation for the first derivative at $x_{i+1/2}$ and $x_{i-1/2}$. This approximations are going to be useful for the approximation of the second derivative.

The first derivative at $x_{i+1/2}$ (Equation 2.67) is going to be found by a centered approximation, so forward and backward approximations are subtracted.

$$\phi(x_{i+1}) = \phi(x_{i+1/2}) + (x_{i+1} - x_{i+1/2})\left(\frac{\delta\phi}{\delta x}\right)_{i+1/2}$$

$$\phi(x_i) = \phi(x_{i+1/2}) + (x_i - x_{i+1/2})\left(\frac{\delta\phi}{\delta x}\right)_{i+1/2}$$

$$\left(\frac{\delta\phi}{\delta x}\right)_{i+1/2} = \frac{\phi(x_{i+1}) - \phi(x_i)}{x_{i+1} - x_i} \tag{2.67}$$

Following the same procedure the approximation for $x_{i-1/2}$ is found (Equation 2.68).

$$\left(\frac{\delta\phi}{\delta x}\right)_{i-1/2} = \frac{\phi(x_i) - \phi(x_{i-1})}{x_i - x_{i-1}} \tag{2.68}$$

Approximation second derivative

In Equation 2.60, the approximation of the second derivative is required. Equations 2.69 and 2.70 depicts the approximation for centered differences.

$$\left(\frac{\delta^2\phi}{\delta x^2}\right)_i = \frac{\left(\frac{\delta\phi}{\delta x}\right)_{i+1} - \left(\frac{\delta\phi}{\delta x}\right)_{i-1}}{x_{i+1} - x_{i-1}} \tag{2.69}$$

$$\left(\frac{\partial^2\phi}{\partial x^2}\right)_i = \frac{\phi_{i+2} - 2\phi_i + \phi_{i-2}}{(x_{i+1} - x_{i-1})^2} \tag{2.70}$$

Additionally, an equation for the second derivative by approximating first derivatives in $i+1/2$ and $i-1/2$ (Equation 2.71) is found.

$$\left(\frac{\delta^2\phi}{\delta x^2}\right)_i = \frac{\left(\frac{\delta\phi}{\delta x}\right)_{i+1/2} - \left(\frac{\delta\phi}{\delta x}\right)_{i-1/2}}{\frac{x_{i+1} - x_{i-1}}{2}} \tag{2.71}$$

Equations 2.68 and 2.67 are replaced in Equation 2.71. Constant space discretization is considered so that $x_{i+1} - x_i = x_i - x_{i-1} = \frac{(x_{i+1} - x_{i-1})}{2} = \Delta x$, so Equation 2.72 is found.

$$\frac{\partial^2\phi}{\partial x^2} = \frac{\phi_{i+1} - 2\phi_i + \phi_{i-1}}{\Delta x^2} \tag{2.72}$$

Truncation Error Differential equations can be approximate with forward, backward, or central finite differences. The main change between these approximations is the error done in the approximation. According to [22], this is a **truncation error** due to the terms omitted in Taylor series expansion. The truncation error is given by Equation 2.73.

$$\varepsilon_T = (\Delta x)^m \alpha_{m+1} + (\Delta x)^{m+1} \alpha_{m+2} + \cdots + (\Delta x)^n \alpha_{n+1} \tag{2.73}$$

Where:

Δx is the spacial step (m)

α represents the constant values as well as the derivatives of higher order ($\frac{1}{s}$)

Since; Δx is supposed to be small, then the biggest and dominant term is the one with the smallest exponent. This structure can be seen in Equation 2.63.

For the case of a forward or backward approximation, the error (if Δx is small enough) has an order $O(\delta x)$. This order means that by halving the step size the error decrease by 1/2. Equation 2.63 shows a dominant term powered to 1.

A central difference has a error with order $O(\delta x^2)$, so if the step size is divided by two, the error will be reduced by 4. This error order is illustrated in Equation 2.74 where the dominant element in the truncation process is powered to two.

$$\left(\frac{\partial\phi}{\partial x}\right)_i = \frac{\phi_{i+1} - \phi_{i-1}}{x_{i+1} - x_{i-1}} - \frac{(x_{i+1} - x_i)^2 - (x_i - x_{i-1})^2}{2(x_{i+1} - x_{i-1})}\frac{\partial^2\phi}{\partial x^2} + HOT \tag{2.74}$$

Based on the truncation analysis some conclusions can be drawn:

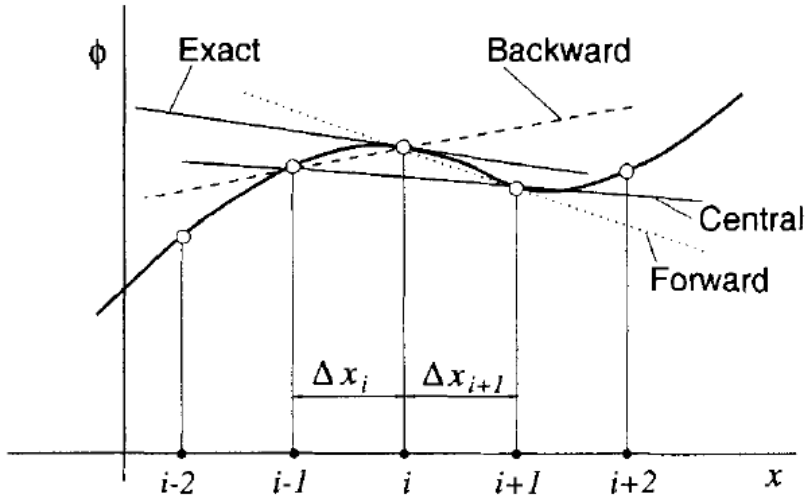

Figure 2.36: Approximations for the first derivative (Image taken from [22])

1. Differential equations are better approximate by central differences (With a small δx)
2. Central differences have less error when its components are analyzed in $i+1/2$ and $i-1/2$ due to a smaller δx.

Figure 2.36 shows graphically the different approximations (Forward, backward, and central). Central difference portrays a better approximation over forward or backward approximation.

Equation Analysis Non-Staggered case

In order to solve Poisson equation, [23] propose the discrete approximation presented in Equation 2.75.

$$\frac{P_{i+1}^{n+1} - 2P_i^{n+1} + P_{i-1}^{n+1}}{\Delta x^2} = \frac{\rho}{\Delta t} \cdot \frac{U_{x_{i+1/2}}^n - U_{x_{i-1/2}}^n}{\Delta x} \tag{2.75}$$

The discrete approximation to solve the Poisson equation has a centered discretization scheme where first derivatives are analyzed at $i+1/2$ and $i-1/2$. According to [19], to keep consistency in the discretization of Poisson equation is necessary. In order to reduce the error in the process to obtain $U_{x_{i+1/2}}^n$ [23] provides an expression for it (Equation 2.76).

$$U_{x_{i+1/2}}^n = \frac{1}{2} \cdot \left[\left(U_{x_{i+1}}^n + \Delta t \frac{P_{i+2}^{n+1} - P_i^{n+1}}{2 \cdot \Delta x} \right) + \left(U_{x_i}^{n+1} + \Delta t \frac{P_{i+1}^{n+1} - P_{i-1}^{n+1}}{2 \cdot \Delta x} \right) \right] - \frac{\Delta t \cdot \left(P_{i+1}^{n+1} - P_i^{n+1} \right)}{\Delta x} \tag{2.76}$$

Once the Poisson equation is solved the velocities are corrected, this time taking into account the pressure terms.

$$U_x^{n+1} = U_x^n - \frac{\Delta t}{\rho} \cdot \nabla P^{n+1} \tag{2.77}$$

This equation is then transform into a discrete form:

$$U_x^{n+1} = U_x^n - \frac{\Delta t}{\rho} \cdot \frac{P_{i+1}^{n+1} - P_{i-1}^{n+1}}{2 \cdot \Delta x} \tag{2.78}$$

An alternative discretization scheme is proposed by [23]. This discretization is characterized by the reduction of error in the discretization of the momentum equation:

$$\frac{P_{i+2}^{n+1} - 2P_i^{n+1} + P_{i-2}^{n+1}}{4 \cdot \Delta x^2} = \frac{\rho}{\Delta t} \cdot \frac{U_{x_{i+1/2}}^n - U_{x_{i-1/2}}^n}{\Delta x} \tag{2.79}$$

This last discretization coincides with the discretization proposes by [24]. Based on Figure 2.37:

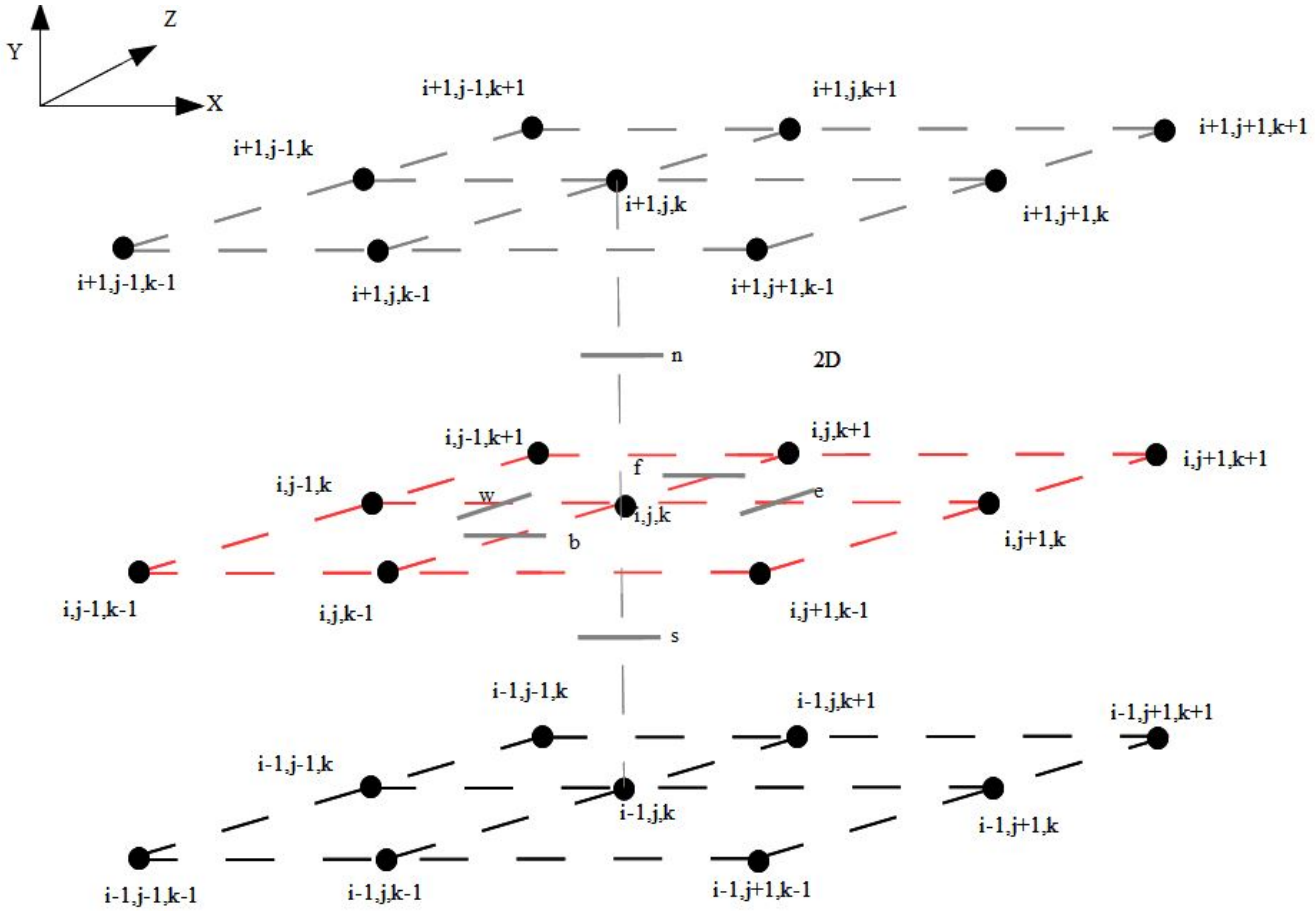

Figure 2.37: Scheme for discretization

$$\frac{\partial^2 P}{\partial x^2} - \frac{\rho}{\Delta t} \cdot \frac{\partial U_x}{\partial x} = 0$$

$$\frac{\partial}{\partial x}\left(\frac{\partial P}{\partial x} - \frac{\rho}{\Delta t} \cdot U_x\right) = 0$$

$$\frac{\left(\frac{\partial P}{\partial x} - \frac{\rho}{\Delta t} \cdot U_x\right)_e - \left(\frac{\partial P}{\partial x} - \frac{\rho}{\Delta t} \cdot U_x\right)_w}{\Delta x} = 0$$

$$\theta \cdot P_{i+1}^{n+1} - 2 \cdot \theta \cdot P_i^{n+1} + \theta \cdot P_{i-1}^{n+1} = \frac{\rho}{2} \cdot (U_{x_{i+1}}^n - U_{x_{i-1}}^n); \theta = \frac{\Delta t}{\Delta x} \tag{2.80}$$

Equation 2.80 is the same result as the development of Equation 2.79. Therefore, this is the formulation used in this case. The three dimensional version of this equation (Equation 2.81) is obtained following the same process but with the addition of pressure and velocities components in x and y direction.

$$\frac{\partial^2 P}{\partial x^2} + \frac{\partial^2 P}{\partial y^2} + \frac{\partial^2 P}{\partial z^2} = \frac{\rho}{\Delta t}\left(\frac{\partial U_x}{\partial x} + \frac{\partial U_y}{\partial y} + \frac{\partial U_z}{\partial z}\right)$$

$$\frac{\partial}{\partial x}\left(\frac{\partial P}{\partial x} - \frac{\rho}{\Delta t} U_x\right) + \frac{\partial}{\partial y}\left(\frac{\partial P}{\partial y} - \frac{\rho}{\Delta t} U_y\right) + \frac{\partial}{\partial z}\left(\frac{\partial P}{\partial z} - \frac{\rho}{\Delta t} U_z\right) = 0$$

$$\theta_x P_{i+1,j,k}^{n+1} - 2\theta_x P_{i,j,k}^{n+1} + \theta_x P_{i-1,j,k}^{n+1} + \theta_y P_{i,j+1,k}^{n+1} - 2\theta_y P_{i,j,k}^{n+1} + \theta_y P_{i,j-1,k}^{n+1} + \theta_z P_{i,j,k+1}^{n+1} - 2\theta_z P_{i,j,k}^{n+1} + \theta_z P_{i,j,k-1}^{n+1} =$$

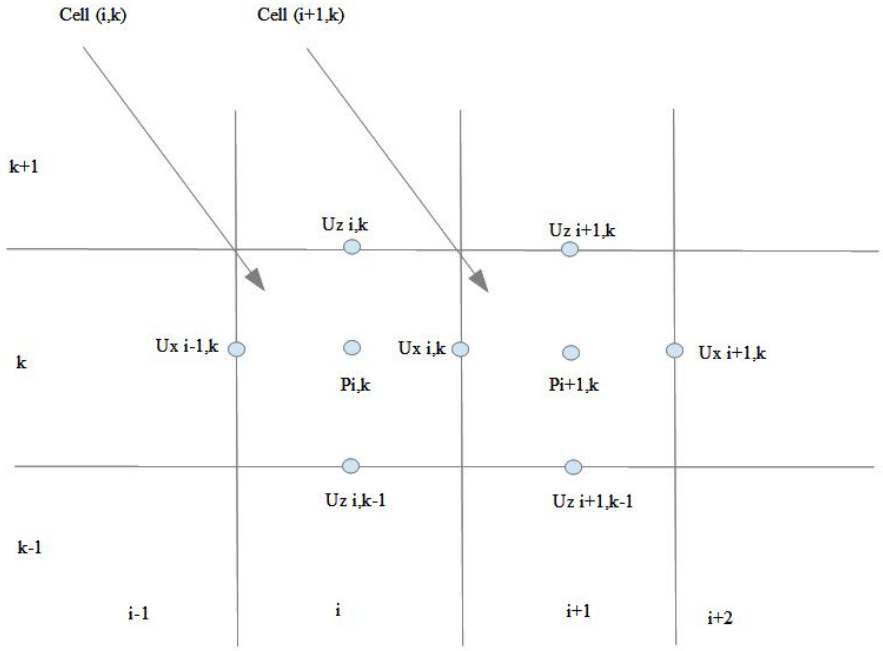

Figure 2.38: Staggered Grid (Image taken from [28])

$$\frac{U^n_{x_{i+1,j,k}} - U^n_{x_{i-1,j,k}}}{2\Delta x} + \frac{U^n_{x_{i,j+1,k}} - U^n_{x_{i,j-1,k}}}{2\Delta y} + \frac{U^n_{x_{i,j,k+1}} - U^n_{x_{i,j,k-1}}}{2\Delta z}$$

$$\theta_x = \frac{\Delta t}{\Delta x^2}; \theta_y = \frac{\Delta t}{\Delta y^2}; \theta_z = \frac{\Delta t}{\Delta z^2}; U^*_x = \rho U_x; U^*_y = \rho U_y; U^*_z = \rho U_z \tag{2.81}$$

Boundary Conditions Non-staggered case

Due to the use of an CFD problem, it is necessary to have boundary conditions. Neumann boundary condition have been applied as suggested [24] [25] and [26]. Neumann boundary conditions are the impose of a value of the ordinary derivative at the boundary: Pressure derivative in the present case. [27] states that since Poisson equation was derived from the momentum equation, it makes sense to derive an equation for the boundary condition. The solution is to apply the normal component of the momentum equation at the boundary, taking into account that this condition needs to be an scalar. Additionally, following the procedure based on the analysis done in Figure 2.37, near the boundary of the domain at i=2 and i=m-1, where m is the position of the end of the analyzed section, the derivatives of the pressure are analyzed at $i = 1 + 1/2$ and $i = m - 1/2$. For this reason the boundary condition is analyzed at these points [24]. The boundary conditions for 2-D case are presented in Equation 2.82.

$$\frac{\partial P}{\partial x} = 0|_{i=1+1/2}; \frac{\partial P}{\partial y} = 0|_{j=1+1/2}; \frac{\partial P}{\partial x} = 0|_{i=n-1/2}; \frac{\partial P}{\partial y} = 0|_{j=m-1/2} \tag{2.82}$$

Observations for non-staggered system Water is considered as incompressible and the continuity equation only provides an equation for its gradient. In this way, when this system is solved there is no way to calculate the absolute pressure. This causes that the system $A[T] = b$ cannot be solved directly because **A** is singular [17]. A solution is to impose a pressure at any point of the domain so that the rest of points converge to that pressure.

EQUATION DISCRETIZATION STAGGERED CASE

The staggered grid variables are stored at different points. The domain is analyzed through cells because of convenience (Figure 2.38). Pressure is saved at the center of the cell while velocities are store at the boundaries. [28] states that due to this variables arrangement, in which some variable are at the boundaries and others not an additional strip needs to be added for the boundary conditions (Figure 2.39).

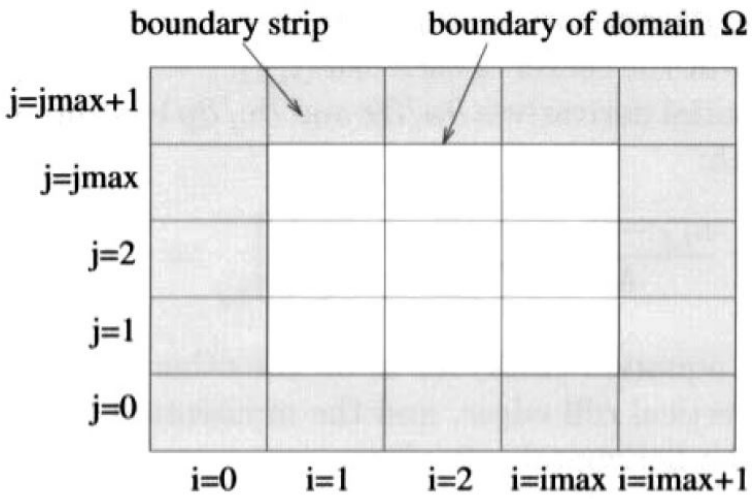

Figure 2.39: Additional strip in domain (Image adapted from [28])

Approximation to the first derivative

Following the nomenclature presented in Figure 2.38, the first derivative for U_x is approximated with Equation 2.83.

$$\left(\frac{\partial U_x}{\partial x}\right)_i = \frac{U_{x_i} - U_{x_{i-1}}}{\Delta x} \tag{2.83}$$

For pressure the equation is:

$$\left(\frac{\partial P}{\partial x}\right)_i = \frac{P_{i+1} - P_i}{\Delta x} \tag{2.84}$$

Approximation to the second derivative

The second derivative for U_x is given by Equation 2.85.

$$\left(\frac{\partial^2 U_x}{\partial x^2}\right)_i = \frac{U_{x_{i+1}} - 2U_{x_i} + U_{x_{i-1}}}{\Delta x^2} \tag{2.85}$$

Pressure second derivative is approximate with Equation 2.86.

$$\left(\frac{\partial^2 P}{\partial x^2}\right)_i = \frac{P_{i+1} - 2P_i + P_{i-1}}{\Delta x^2} \tag{2.86}$$

Equation Analysis

Equation 2.87 illustrate the approximation used for staggered grid.

$$\nabla^2 P^{n+1} = \frac{\rho \cdot \nabla U^n}{\Delta t}$$

$$\left(\frac{\partial^2 P}{\partial x^2}\right)_{i,j,k} + \left(\frac{\partial^2 P}{\partial y^2}\right)_{i,j,k} + \left(\frac{\partial^2 P}{\partial z^2}\right)_{i,j,k} = \frac{\rho}{\Delta t}\left(\left(\frac{\partial U_x}{\partial x}\right)_{i,j,k} + \left(\frac{\partial U_y}{\partial y}\right)_{i,j,k} + \left(\frac{\partial U_z}{\partial z}\right)_{i,j,k}\right)$$

$$\frac{P^{n+1}_{i+1,j,k} - 2P^{n+1}_{i,j,k} + P^{n+1}_{i-1,j,k}}{\Delta x^2} + \frac{P^{n+1}_{i,j+1,k} - 2P^{n+1}_{i,j,k} + P^{n+1}_{i,j-1,k}}{\Delta y^2} + \frac{P^{n+1}_{i,j,k+1} - 2P^{n+1}_{i,j,k} + P^{n+1}_{i,j,k-1}}{\Delta z^2}$$

$$= \frac{\rho}{\Delta t}\left(\frac{U^n_{x_{i,j,k}} - U^n_{x_{i-1,j,k}}}{\Delta x} + \frac{U^n_{y_{i,j,k}} - U^n_{y_{i,j-1,k}}}{\Delta y} + \frac{U^n_{z_{i,j,k}} - U^n_{z_{i,j,k-1}}}{\Delta z}\right) \tag{2.87}$$

Boundary conditions

Velocities: In the inflow part the velocities are not allowed to be changed, so in the script they are fixed or with restricted changes.

Pressure: [28] demonstrates that the required boundary condition for this case is to equalize the boundary strip pressure with its neighbor at the inside the domain.

$$P_{0,j,k} = P_{1,j,k}; P_{i\max+1,j,k} = P_{i\max,j,k}$$
$$P_{i,0,k} = P_{i,1,k}; P_{i,j\max+1,k} = P_{i,j\max,k}$$
$$P_{i,j,0} = P_{i,j,1}; P_{i,j,k\max+1} = 0$$

Observations for staggered system

In case of replacing the boundary conditions directly in Poisson equation (Equation 2.87) the resulting equation system is singular. In order to overcome the singularity [28] suggest to satisfy the boundary conditions, by forcing the pressures at the boundary strip to be the same as in the domain.

Convergence criteria The criteria of convergence to stop the iterations is based on a comparison of the data corrected and the previous value. When two consecutive values does not change significantly, the system has found a solution. The convergence formulation is given by Equation 2.88.

$$Tolerance = \left| \frac{U^{n+1} - U^n}{U^n} \right| \cdot 100 \tag{2.88}$$

For both runnings, staggered and non-staggered, the criteria to stop the iterations was a tolerance of 0.1 %.

2.3. DISCRETIZATION STABILITY ANALYSIS

In order to determine the stability of the different schemes (Staggered and non-staggered), an analysis (based on [29]) was performed. The procedure consists on applying the solutions of the difference equation and resolvent equation.

When differential equations are approximate with Finite Difference Elements, the result is a difference equation. A difference equation is an equation where a term is function of the previous terms [30]. A general expression of a difference equation is given by Equation 2.89.

$$X_n = X_{n-1} + X_{n-2} \tag{2.89}$$

A difference equation is considered as linear when each term is a liner function of the preceding terms. According to [29] the general solution of such equations is Equation 2.90.

$$P_i^{n+1} = r^{n+1}\widetilde{P_i} \tag{2.90}$$

Where:
r is a constant
$\widetilde{P_i}$ is a coefficient

When replacing Equation 2.90 into the differential equation, an mathematical expression called Resolvent equation is obtained. This equation has a general solution (Equation 2.91) given by [31].

$$\widetilde{P_i} = a \cdot z^i \tag{2.91}$$

Where:
a: is a constant value
z: represents the roots of the equation

Equation 2.92 show the final solution of the difference equation.

$$P_i^{n+1} = a \cdot r^{n+1} \cdot z^i \tag{2.92}$$

The stability analysis is done by finding the roots (z). The system is stable when z is positive, however a negative root indicate the system will suffer oscillations [29].

To illustrate the presence of oscillations is necessary the **characteristics** concept. Characteristics are curves which shows the position and time where a disturbance is [32]. By definition an observer moving with a velocity $\frac{dz}{dt}$ do not see a change in Riemann invariants (For 1-D case without taking into account Friction and assuming hydrostatic pressure distribution Riemann invariants=U +/−c where c is the wave velocity (m/s), Figure 2.40).

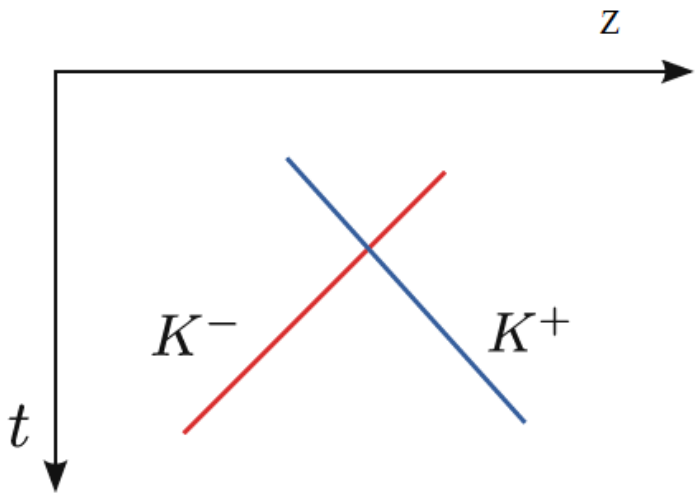

Figure 2.40: Characteristic lines (K^+,K^-) in plane z-t (Image taking from [32])

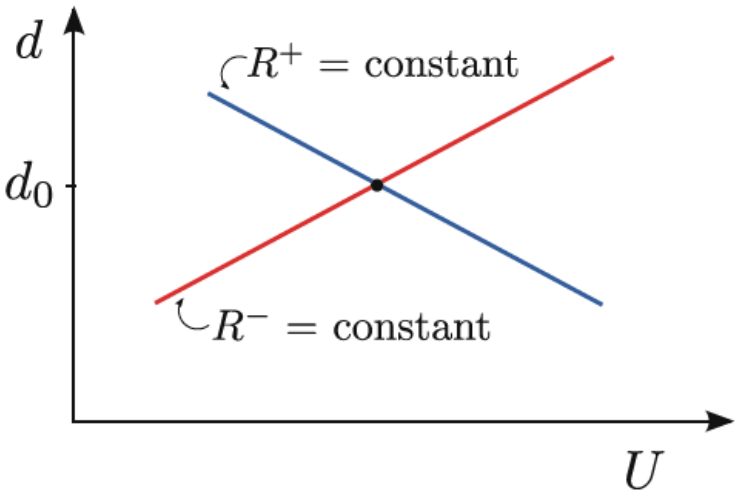

Figure 2.41: State diagram (R^+ and R^- Riemann variables) (Imagen taken from [32])

Another scheme necessary is the state diagram (Figure 2.41). This Figure depicts the flow condition (Water depth d, Velocity U) for each sub domain in the z-t diagram.

In order to clarify the previous concept a simple example is presented. Figure 2.42(a) shows a flume infinite long with no velocity. There is a gate separating two sides of the flume with different water depths (I(d_1,U=0),II(d_2,U=0)). Suddenly, the gate is removed, water depth and velocity needs to be known in space and time. In the gate point there is a discontinuity producing two characteristics (Figure 2.42(b)). Taking the characteristcs from I and II a third state is found (III (d_3,U=U_3)). The flow states can be seen in Figure 2.42(c). In the characteristic Figure (Figure 2.42(b)) line A-A shows that is possible to track the flow state at certain point through time. Line B-B (Figure 2.42(b)) depicts the flow state at a certain moment in the whole domain.

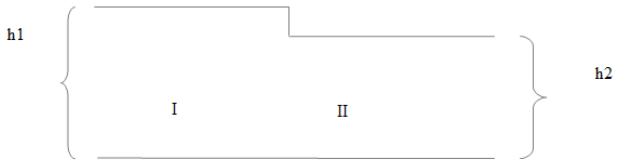

(a) Scheme

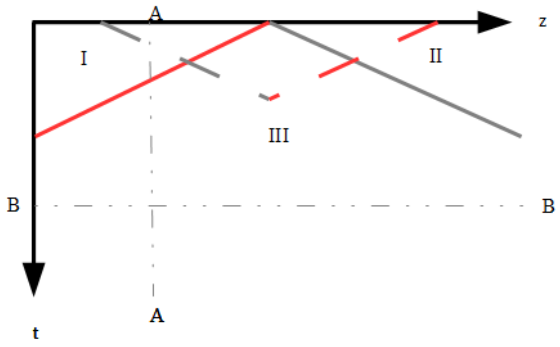

(b) z-t plane

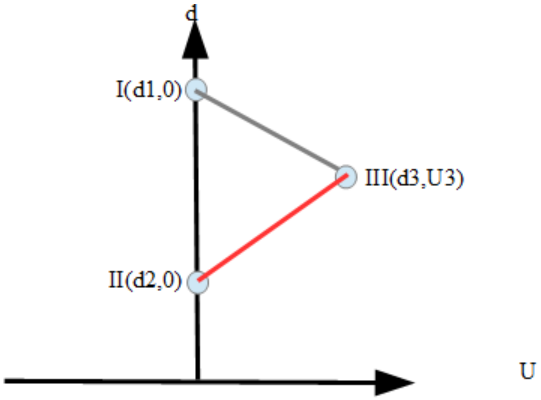

(c) State diagram

Figure 2.42: Example for characteristics aplication

For the current work, the velocity field to obtain is constant in time, so there is no a disturbance traveling along the flume ($\frac{dz}{dt} = 0$). The domain has been discretized, producing n points. The characteristic lines are shown in Figure 2.43.

To create the state diagram the solution of the velocity at each node based Equation 2.92 has the form presented in Equation 2.93.

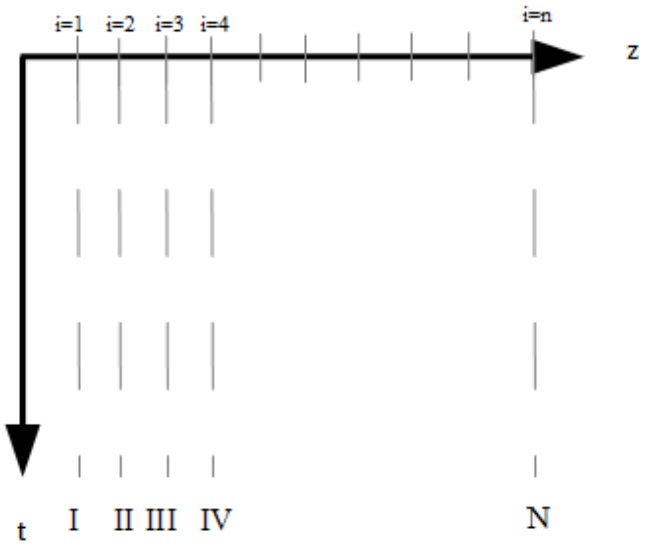

Figure 2.43: Characteristics for the current study case

$$U_i^n = a \cdot r^n \cdot z_1^i + a \cdot r^n \cdot z_2^i \tag{2.93}$$

Two cases are important for stability. The first case to analyze is what happens when z1=z2=1. Another assumption is a constant water depth (d1 in Figure 2.44) along the flume. In that case U is going to have a stable value (U1 in Figure 2.44) for every discretized space point i (Figure 2.45).

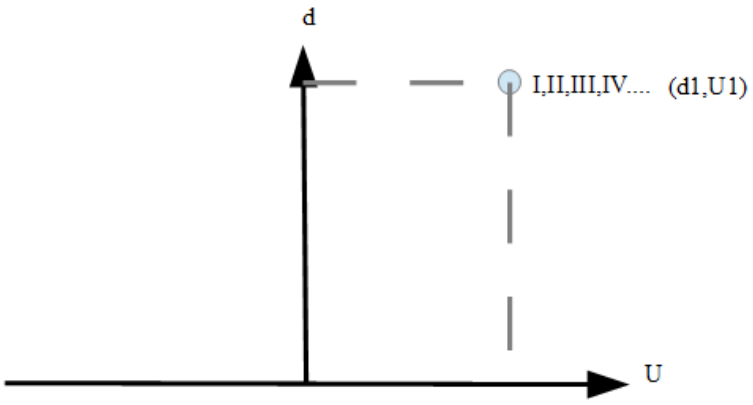

Figure 2.44: State diagram when roots are positive

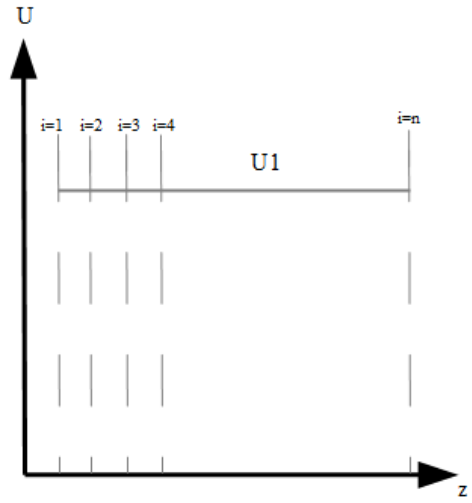

Figure 2.45: U-z plane showing a straight line (no oscillations)

The second case is when z1 has a value of 1 value and z2 is -1 (Constant water depth supposition is used in this case as well). Equation 2.93 indicates for even i values U (U1 in Figure 2.46) has one state, but for odd i values the term $a \cdot r^n \cdot z_2^i$ has a negative value which produce other U value (U2 in Figure 2.46). Figure 2.47 shows that each 2 i values (equivalent to 2 Δx) the system has the same state, the form of these phenomena is a oscillation with a wave length of 2 Δx.

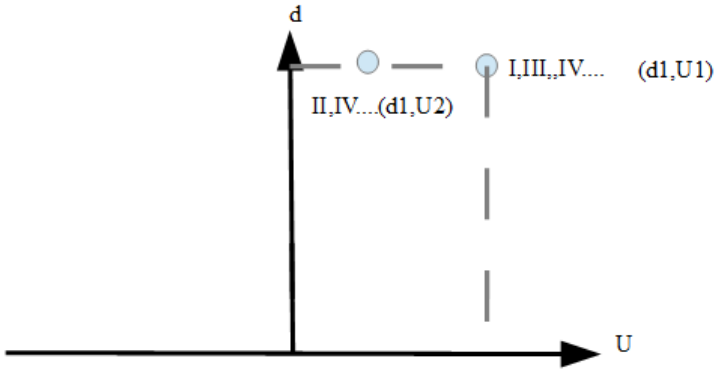

Figure 2.46: State diagram when there is one positive root and a negative one

From the cases studied, if root is 1 then the system is stable, but a root of -1 generates oscillations.

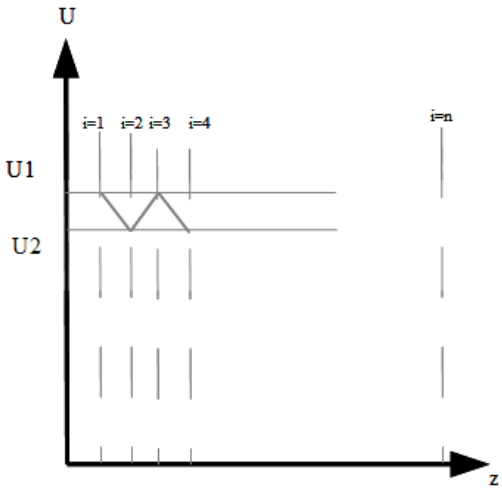

Figure 2.47: U-z plane showing oscillations

2.3.1. NON-STAGGERED GRID FIRST DERIVATIVES ANALYZED $i+1$ AND $i-1$

The 1-D Poisson Equation is given by Equation 2.94.

$$\frac{\partial^2 P}{\partial x^2} - \frac{\rho}{\Delta t} \cdot \frac{\partial U}{\partial x} = 0 \tag{2.94}$$

Equation 2.94 is discretized obtaining Equation2.95:

$$\frac{P_{i+2}^{n+1} - 2P_i^{n+1} + P_{i-2}^{n+1}}{4 \cdot \Delta x^2} - \frac{\rho}{\Delta t} \cdot \left(\frac{U_{i+1}^n - U_{i-1}^n}{2 \cdot \Delta x} \right) = 0 \tag{2.95}$$

The correction formula is presented in Equation 2.96.

$$\frac{\partial P}{\partial x} + \frac{\partial U}{\partial t} \cdot \rho = 0 \tag{2.96}$$

Equation 2.96 is approximate with Equation 2.97.

$$\frac{P_{i+1}^{n+1} - P_{i-1}^{n+1}}{2 \cdot \Delta x} + \frac{U_i^{n+1} - U_{i-1}^n}{\Delta t} \cdot \rho = 0 \tag{2.97}$$

The solution of a linear difference equation with linear coefficients have the form of Equations 2.98 and 2.99. These solutions are replaced in Equations 2.94 and 2.96 obtaining Equations 2.100 and 2.101.

$$P_i^{n+1} = r^{n+1} \cdot \widetilde{P}_i \tag{2.98}$$

$$U_i^n = r^n \cdot \widetilde{U}_i \tag{2.99}$$

$$r \cdot \frac{\widetilde{P_{i+2}} - 2\widetilde{P_i} + \widetilde{P_{i-2}}}{4 \cdot \Delta x^2} - \frac{\rho}{\Delta t} \cdot \left(\frac{\widetilde{U_{i+1}} - \widetilde{U_{i-1}}}{2 \cdot \Delta x} \right) = 0 \tag{2.100}$$

$$r \cdot \frac{\widetilde{P_{i+1}} - \widetilde{P_{i-1}}}{2 \cdot \Delta x} + \frac{r\widetilde{U_i} - \widetilde{U_i}}{\Delta t} \cdot \rho = 0 \tag{2.101}$$

The resolvent equations (Equations 2.100 and 2.101) has the form of Equations 2.102 and 2.103

$$\widetilde{P_i} = a_1 \cdot z_1^i + a_2 \cdot z_2^i \tag{2.102}$$

$$\widetilde{U_i} = C(a_1 \cdot z_1^i + a_2 \cdot z_2^i) \tag{2.103}$$

The system to solve is presented in Equation 2.104. This system has a shape $A \cdot x = 0$. In order to avoid the solution x=0, A must not be reversible. This condition is attain when the determinant of A is equal to zero.

$$\begin{pmatrix} r \cdot \frac{z^{i+2} - 2z^i + z^{i-2}}{4\Delta x^2} & -\frac{\rho}{\Delta t \cdot 2 \cdot \Delta x}\left(z^{i+1} - z^{i-1}\right) \\ r \cdot \frac{z^{i+1} - z^{i-1}}{2\Delta x} & \frac{rz^i - z^i}{\Delta t} \cdot \rho \end{pmatrix} \tag{2.104}$$

$$\frac{(z^{i+2} - 2z^i + z^{i-2}) \cdot r \cdot z^i \cdot (r-1)}{4\Delta x^2} \cdot \frac{\rho}{\Delta t} + \frac{\rho}{\Delta t} \cdot r \cdot \frac{1}{4\Delta x^2} \cdot \left(z^{i+1} - z^{i-1}\right)^2 = 0$$

$$\left(z^{2i+2} - 2z^{2i} + z^{2i-2}\right) \cdot (r-1) + \left(z^{2i+2} - 2z^{2i} + z^{2i-2}\right) = 0$$

$$z^4 - 2z^2 + 1 = 0$$

The roots are +1 and -1. In this scheme it can be expected oscillations due to the presence of both roots.

2.3.2. NON-STAGGERED GRID SCHEME USED

Poisson discretization for 1-D is shown in Equation 2.105

$$\frac{P_{i+2}^{n+1} - 2 \cdot P_i^{n+1} + P_{i-2}^{n+1}}{4\Delta x^2} - \frac{1}{\Delta t}\left(\frac{U_{i+1/2}^n - U_{i-1/2}^n}{\Delta x}\right) \tag{2.105}$$

[23] propose a pressure weighted interpolation (Equation 2.106).

$$U_{i+1/2}^n = \frac{1}{2} \cdot \left[\left(\rho \cdot U_{i+1}^n + \Delta t \cdot \frac{P_{i+2}^{n+1} - P_i^{n+1}}{2\Delta x}\right) + \left(\rho \cdot U_i^n + \Delta t \cdot \frac{P_{i+1}^{n+1} - P_{i-1}^{n+1}}{2\Delta x}\right)\right] - \Delta t \frac{P_{i+1}^{n+1} - P_i^{n+1}}{\Delta x} \tag{2.106}$$

Replacing Equation 2.106 into Equation 2.105, the used discrete scheme is obtain (Equation 2.107).

$$\theta_x \cdot P_{i+1}^{n+1} - 2\theta_x P_i^{n+1} + \theta_x P_{i-1}^{n+1} = \frac{\rho \cdot U_{i+1}^n}{2\Delta x} - \frac{\rho \cdot U_{i-1}^n}{2\Delta x} \tag{2.107}$$

$\theta_x = \frac{\Delta t}{\Delta x^2}$

The correction formula discretization is given by Equation 2.108.

$$\frac{P_{i+1}^{n+1} - P_{i-1}^{n+1}}{2\Delta x} + \frac{U_i^{n+1} - U_i^n}{\Delta t}\rho = 0 \tag{2.108}$$

Applying the same solution procedure previously shown, the reultin characteristic equation is Equation 2.109

$$z^4 + \phi z^3 + (-2\phi - 2)z^2 + \phi z + 1 = 0 \tag{2.109}$$

$\phi = 4r - 4$
In order to find if z=-1 is a root of the system, a synthetic division procedure is applied.

1	ϕ	$(-2\phi-2)$	ϕ	1	-1
	-1	$-\phi+1$	$3\phi+1$	$-4\phi-1$	
1	ϕ-1	$-3\phi-1$	$4\phi+1$	-4ϕ	

-1 is a root of the system when r=-1.

2.3.3. STAGGERED GRID SCHEME USED

Poisson discretization for 1-D is shown in Equation 2.110

$$\frac{P_{i+1}^{n+1} - 2P_i^{n+1} + P_{i-1}^{n+1}}{\Delta x^2} - \frac{\rho}{\Delta t}\frac{U_i^n - U_{i-1}^n}{\Delta x} = 0 \tag{2.110}$$

The correction formula discretization is given by Equation 2.111.

$$\frac{P_{i+1}^{n+1} - P_i^{n+1}}{\Delta x} + \frac{U_i^{n+1} - U_i^n}{\Delta t}\rho = 0 \tag{2.111}$$

Likewise the previous sections, the roots are found. Equation 2.112 shows the characteristic equation.

$$z^2 - 2z + 1 = 0 \tag{2.112}$$

The solution of Equation 2.112 is 1. Consequently, the system with an staggered grid is stable.

3

RESULT AND DISCUSSION

3.1. RAW DATA

3.1.1. CLOUD POINT

Figure 3.1 shows raw velocities and their positions recorded by the UB flow and placed according to the method detail in Section 2.2.3.

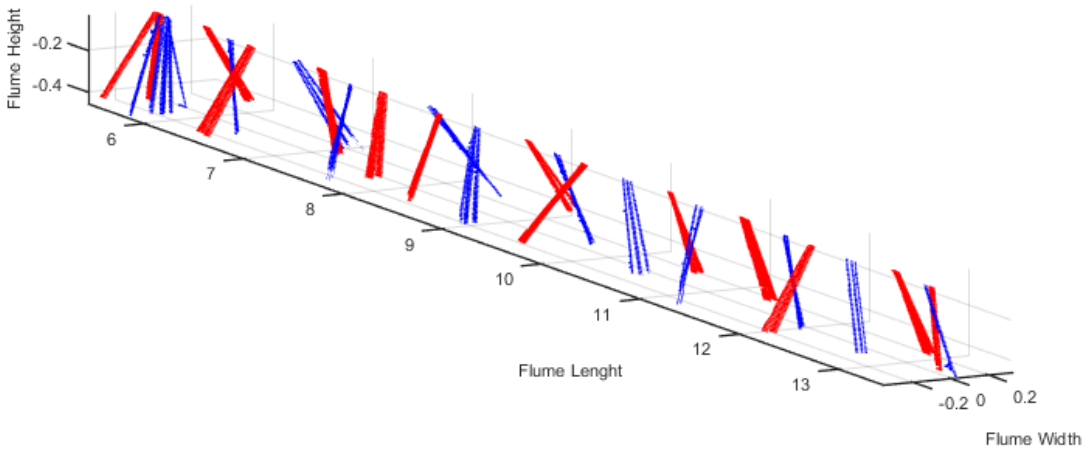

Figure 3.1: UB measurement:blue points are velocities measured through transducer 1, while red points represents data measured by transducer 3

The Figure 3.2 illustrates a basic calculation (triangulation interpolation) of the discharge along the flume with 1-D velocity data (top part). Some non physical explainable oscillations are present. However, these oscillations seem not to be correlated to the UB flow rotation (roll, middle Figure 3.2). The same goes for the

set-up velocity (Bottom Figure 3.2) . Figure 3.2 shows blue and red points. Blue points represents points data taken by transducer 1, while red points represents velocities measured by transducer 3. There is no influence of one transducer over other during the mean flow calculation. However, when only transducer 1 is used (Figure 3.3), the mean flow behaves different. The reason of this difference is the system sensibility to the interpolation procedure applied, so this emphasize the need of an interpolation methodology, which reflects the nature of the flow. In order to know the performance of the methodology validated CFD data have been used. The results are shown in the following section.

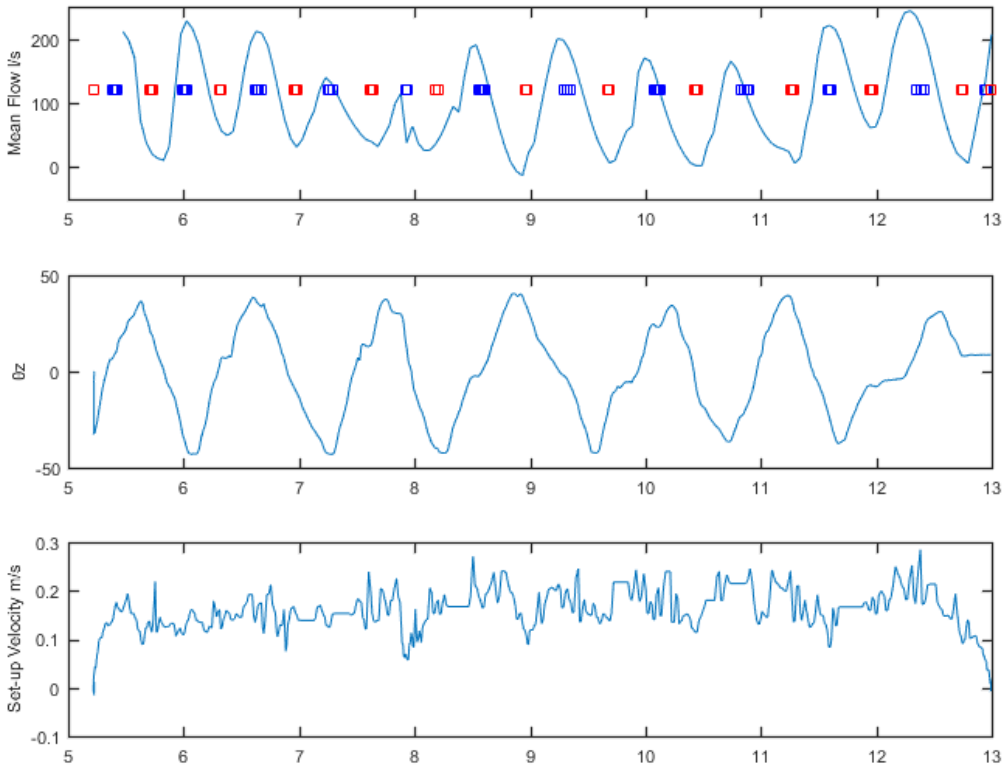

Figure 3.2: Result UB data both transducer used

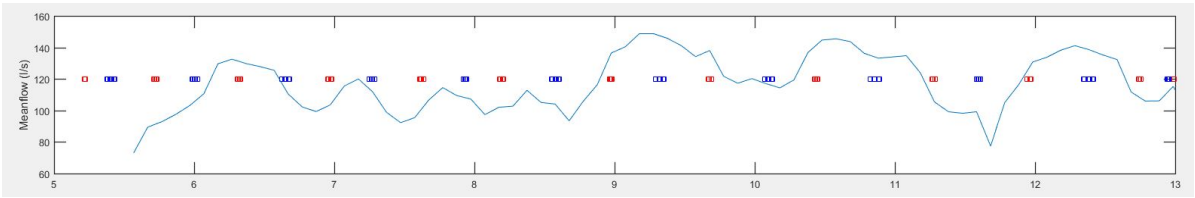

Figure 3.3: Mean flow when only one transducer is used

3.2. CFD DATA

Since the data consist on velocities components in three dimensions as well as the position in x,y, and z. The procedure adapted from [16] and previously described is applied. Nevertheless, there was a small difference: no data preprocessing have been applied to these CFD data. From now on the triangulation based methodology is called Interpolated Data and data obtained with the CFD based interpolation methodology is called Methodology data.

3.2.1. NON-STAGGERED GRID

USE OF THE WHOLE DATA

Isotropic and anisotropic grid were implemented to the CFD data. These grid systems are shown in Figures 3.4(a) and 3.4(b).

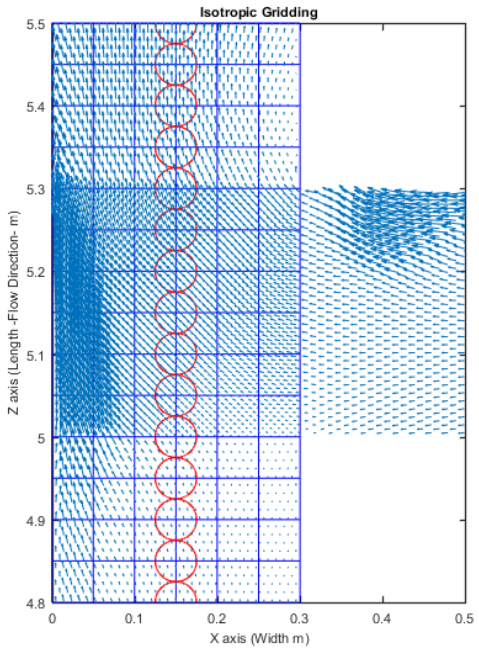

(a) Isotropic Gridding

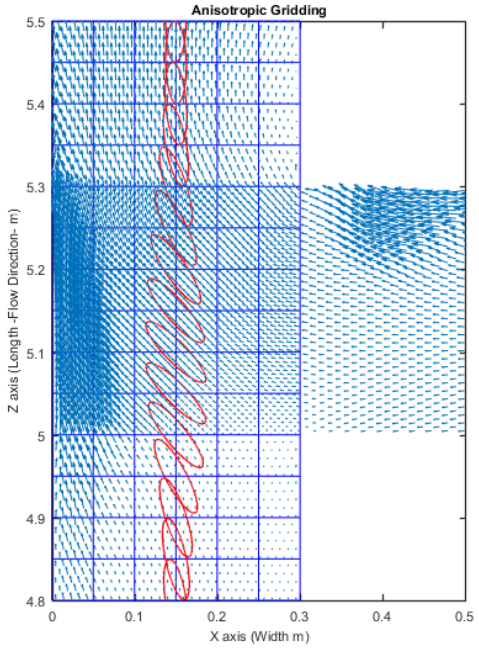

(b) Anisotropic Gridding

Figure 3.4: Left: Isotropic griding, Right: Anisotropic griding

The resulting grid data was the input for the last step: CFD based interpolation.

Figure 3.5 presents a comparison between the CFD data and the data got by the methodology with a tolerance of 0.1 %. This Figure shows the mean flow (y axes) in the cross sections (x axes), the section number increases in downstream direction. In order to calculate flow, the average of the velocities points in one cross section are calculated. This value is multiply by the wet cross section (Equation 3.1) This Figure also depicts two vertical black lines which indicates the location of the intrusion: ending (End) and starting points (Start) of the intrusion. This Figure clearly shows oscillatory values with a $2\Delta x$ wavelength.

$$Flow_k = \left(\sum_{i=1}^{m} \sum_{j=1}^{n} U_{z_{i,j,k}} \right) \cdot Area \tag{3.1}$$

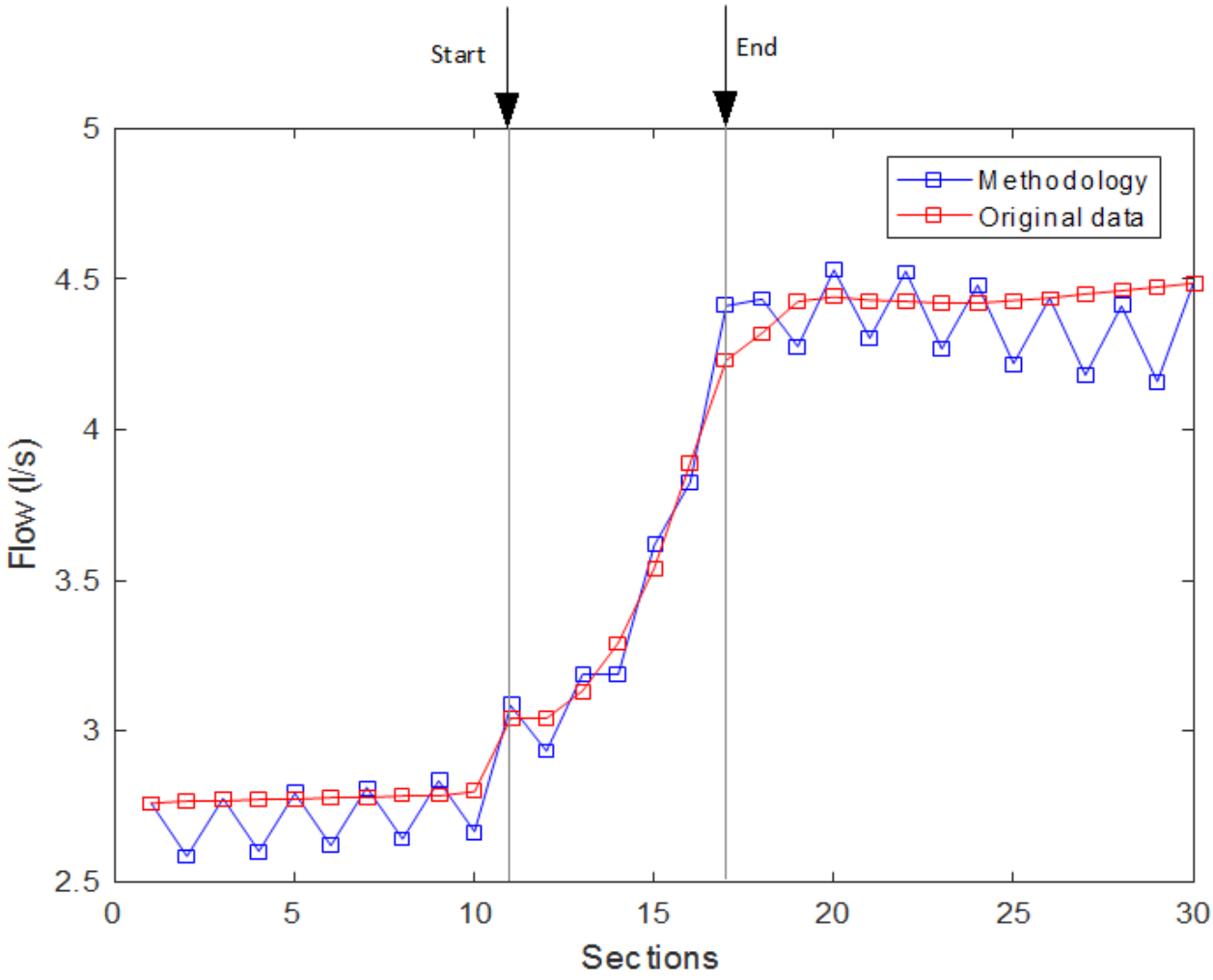

Figure 3.5: Result of methodology when all CFD data is used

SCENARIOS OF DATA SAMPLING

Cross sections withdrawing test

Figure 3.6 depicts the results when cross sections are removed. The results show that as the data removed increased the triangulation based interpolation provide result with no sense. Figure 3.6(c) shows an example where some points predicted by the triangulation based methodology looks like data outliers. The CFD based methodology tends to approximate the original data, but still with oscillations.

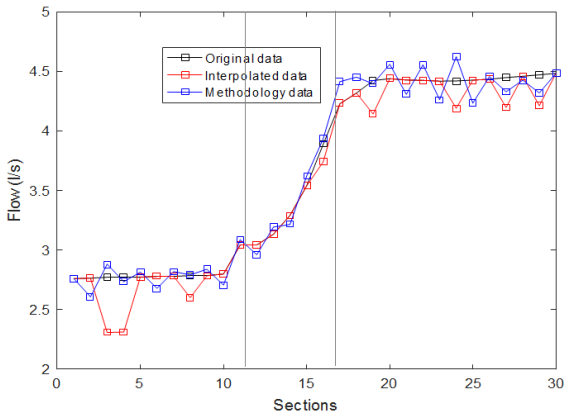

(a) 30 % removal

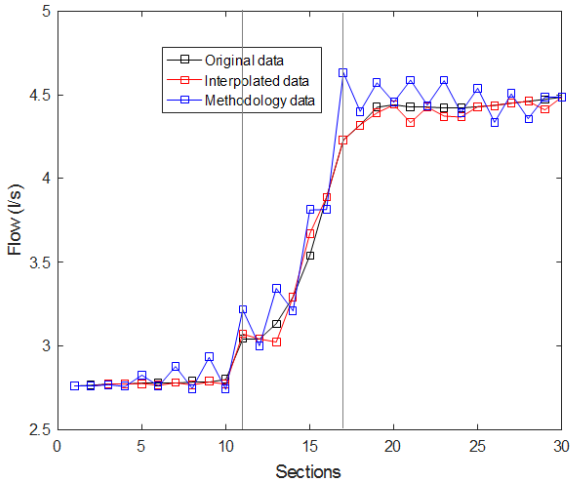

(b) 50 % removal

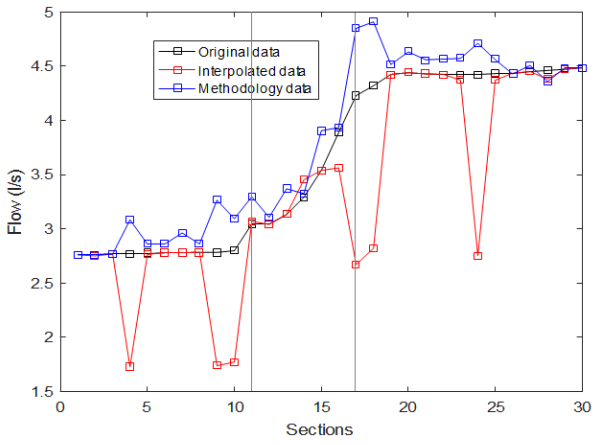

(c) 90 % removal

Figure 3.6: Results cross section section withdrawal test

Sinusoidal movement Data has been subsampled according to the relative UB flow behavior. Figure 3.7 depict different wavelengths (roll angle vs moving speeds).

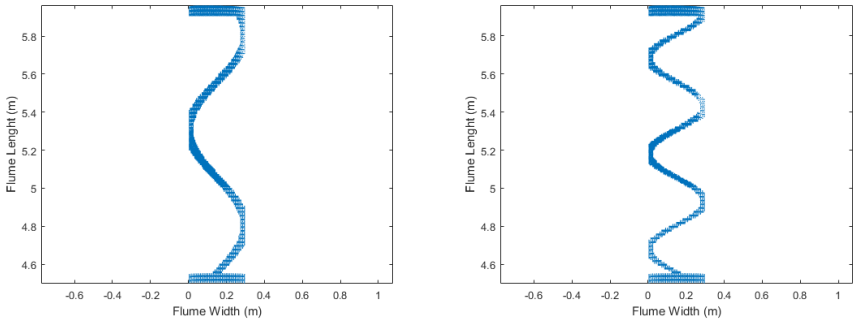

(a) UB flow simulation wavelength 1 m

(b) UB flow simulation wavelength 0.5 m

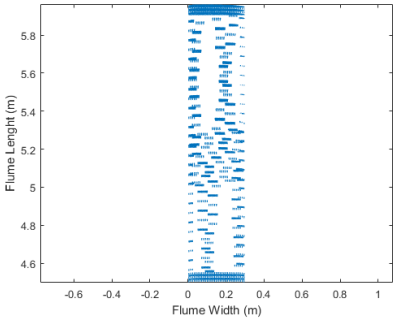

(c) UB flow simulation wavelength 0.05 m

Figure 3.7: Sinusoidal patterns applied during test

Figure 3.8 depicts the result of simulations with different periods of data acquisition. For periods of 1m and 0.5 m (Figures 3.7(a) 3.7(b)) the methodology encounters problems with the data prediction and the problem of 2 Δx oscillations becomes critical. Results seem stable with sub sampling wavelength of 0.05m (Figure 3.7(c)). That case result is good at the beginning but later the problems of oscillations appears again. According to [29], the solution to avoid oscillations is to use a staggered grid.

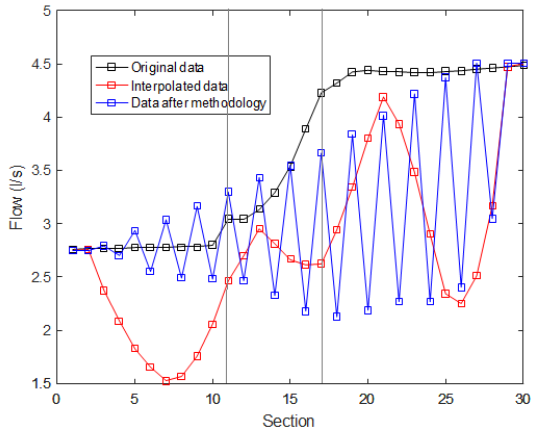

(a) UB flow simulation wavelength 1 m

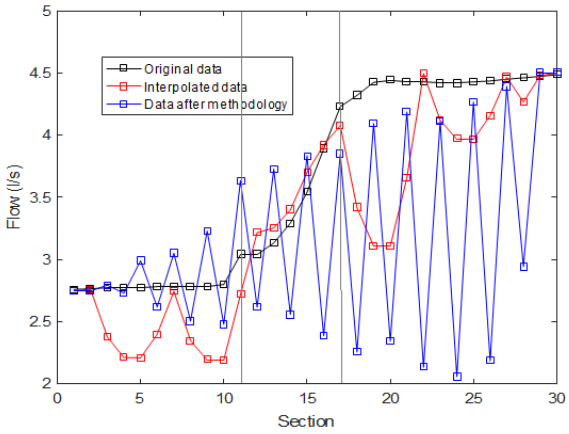

(b) UB flow simulation wavelength 0.5 m

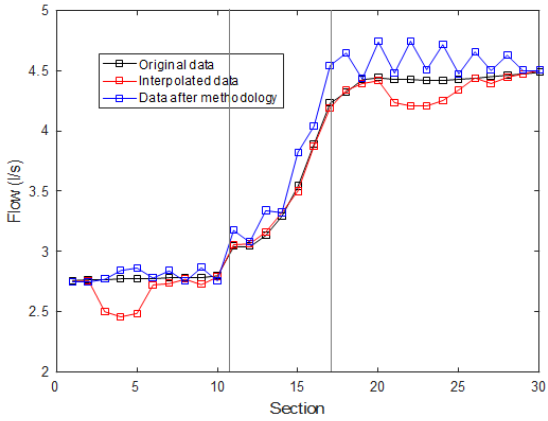

(c) UB flow simulation wavelength 0.05 m

Figure 3.8: Results after sinusoidal pattern applied

3.2.2. STAGGERED GRID

USE OF THE WHOLE DATA

Likewise the non-staggered grid, a isotropic and anisotropic griding are implemented. However, this process was adapted to the staggered scheme. To explain the adaptation is necessary to describe Figure 3.9. This Figure shows the basic structure of a staggered grid, pressure is store in cell center while the velocities components are store at the cell edges as specified. The circumference in the middle of the cell is the isotropic gridding which takes the mean angle of the velocities components inside it. Once an angle has been calculated, an ellipse with the angle previously calculated is created in the point where each of the velocity components is store. The velocities components corresponding to that point inside the ellipse are averaged. In case two ellipse average values coincide in a point, both averaged values are averaged.

To test the stability of the scheme, the previous grid system values were used as initial data for the model. The results are shown in Figure 3.10. The first aspect to be seen is that in contrast with Figure 3.5, in this case there is no 2 Δz oscillations. Another important aspect to analyze is the good approximation with respect to the original data.

SCENARIOS OF DATA SAMPLING

Cross sections elimination When cross sections are removed and a triangulation based interpolation methodology is used to fill data, three elimination cases are analyzed: Remotion of 30%, 50%, and 90%. Figure 3.11 depicts the CFD data (Blue dots) tends to correct the interpolated data based on triangulation methodology (Red data). However, Figure 3.11(d) illustrates the effect of the initial data in the CFD based methodology. In this figure there is a parabola at the beginning, this parabola still exists after the convergence of the methodology, but its amplitude is reduced: First interpolation step (to fulfill the grid) has a strong influence on the

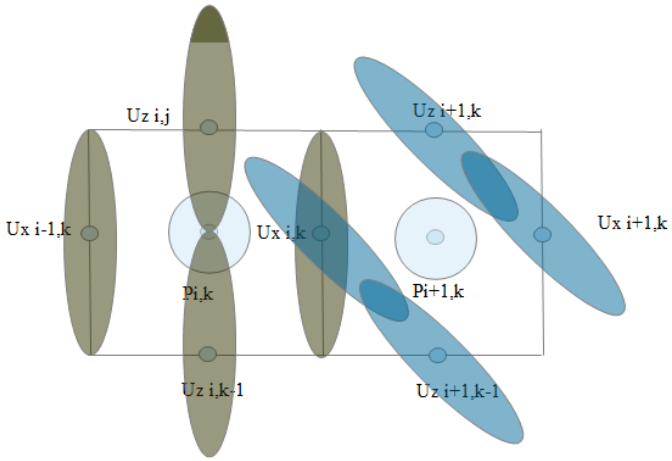

Figure 3.9: Isotropic and anisotropic grid in staggered grid

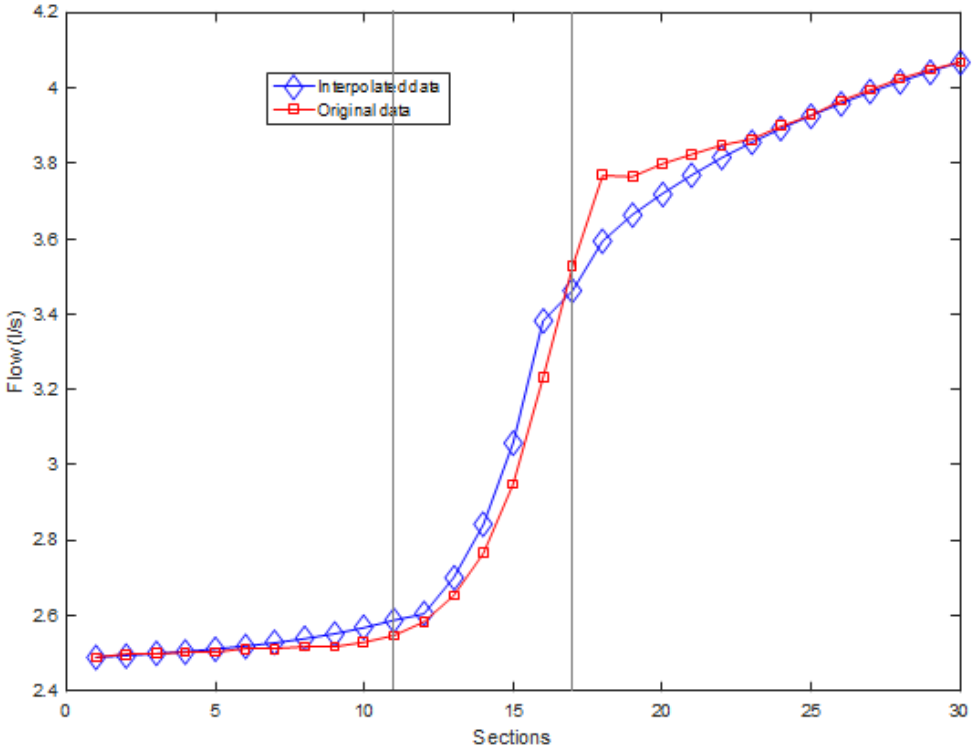

Figure 3.10: Result of data using the whole CFD data

final result.

For the staggered grid, system allows to impose as boundary condition (or fixed values) the measured values. Two cases were analyzed: 1) The measured data was not allowed to be corrected by the methodology (Figures 3.11(b) and 3.11(e)), 2) measured values were allowed to change 10 % with respect to the original value (Figures 3.11(c) and 3.11(f)). Both cases the CFD based interpolation shows an improvement over the geometric based methodology. However, in places where data is not measured there is still the parabolic behavior of the triangulation based interpolation affecting the prediction of the CFD based interpolation methodology. Furthermore, results do not show difference between total and partial restriction.

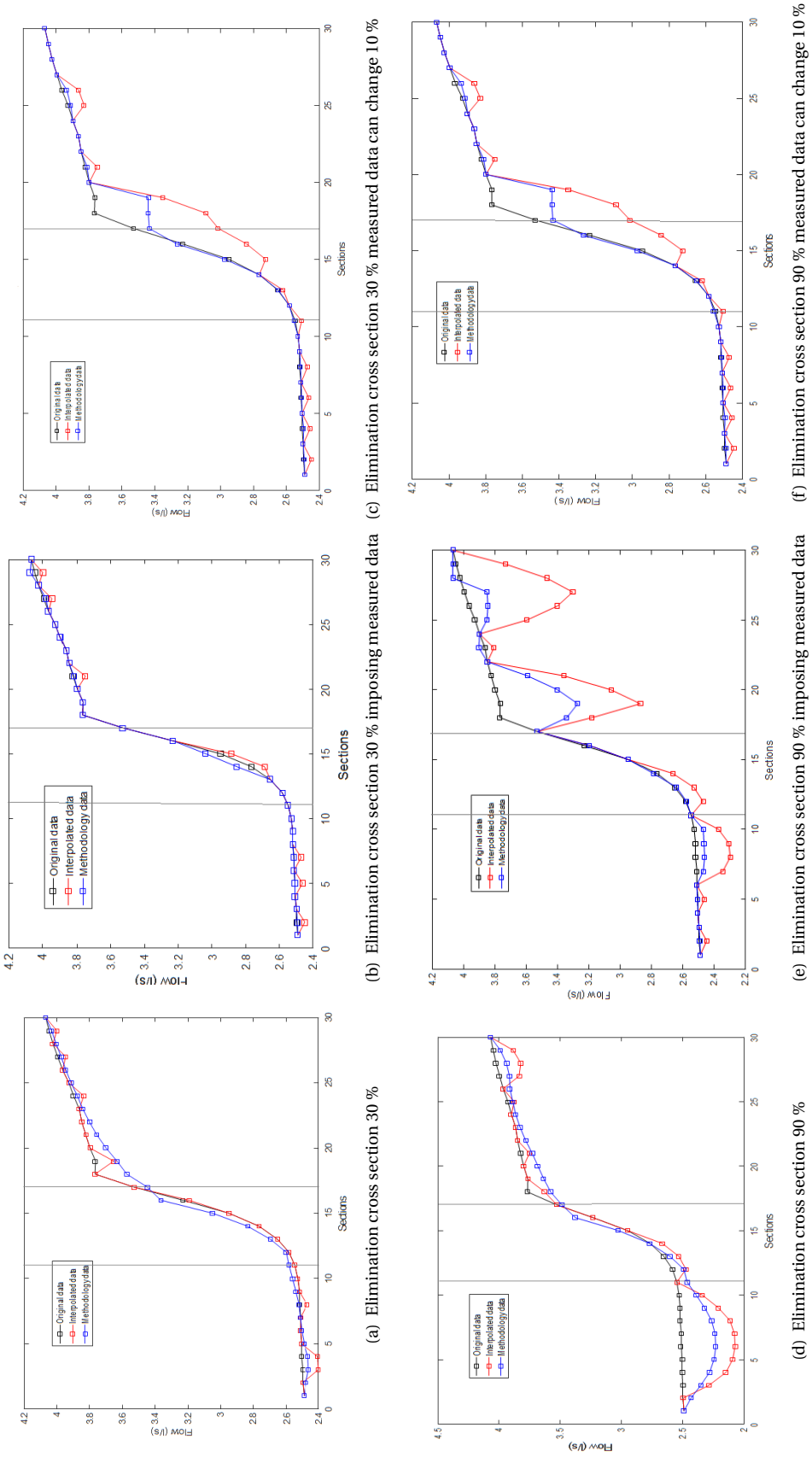

(a) Elimination cross section 30 %

(b) Elimination cross section 30 % imposing measured data

(c) Elimination cross section 30 % measured data can change 10 %

(d) Elimination cross section 90 %

(e) Elimination cross section 90 % imposing measured data

(f) Elimination cross section 90 % measured data can change 10 %

Figure 3.11: Results cross section elimination staggered case

Sinusoidal movement When the UB flow data measurement pattern is analyzed (Figure 3.12(a) and 3.12(d) which represents periods of measurement of 1m and 0.05 m respectively), it shows more stable results than geometric based methodology. Nevertheless, both methodologies have problems to follow the shape of the original curve in the intrusion part. In Figure 3.12(a) it is noticeable the effect of the initial values in the methodology, since there is a parabolic pattern again, but this Figure also depicts the corrections done by the methodology.

Likewise the cross section elimination, in this case the data measured is forced to be boundary condition. It is analyzed the total restriction and the partial restriction. There was no difference between both cases, however it can change with the use of a device since then it is necessary to take into account noise and the accuracy of the instrument. Another important aspect, the data calculated with the CFD methodology provides with better result than the interpolation based on geometry.

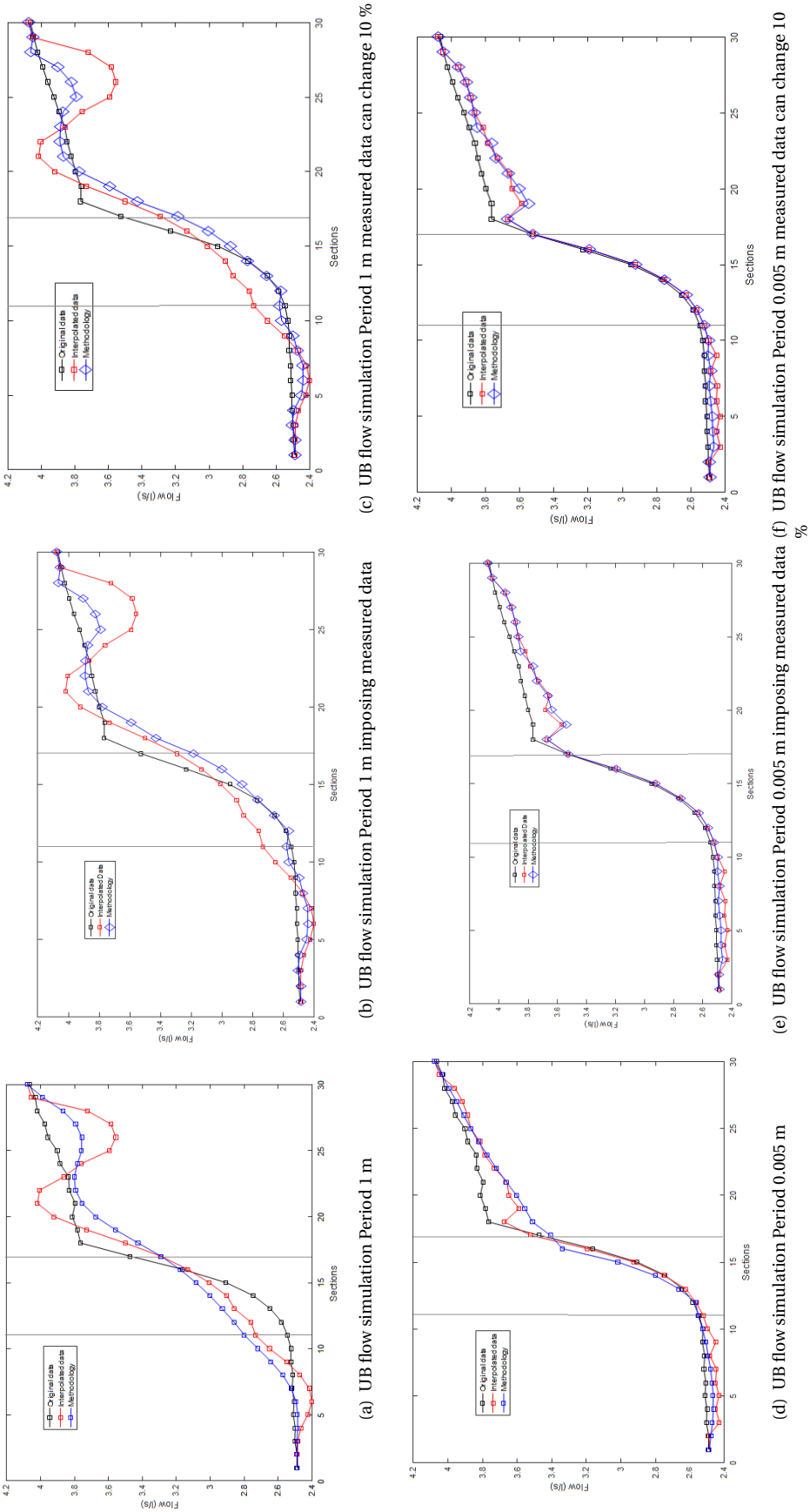

(a) UB flow simulation Period 1 m

(b) UB flow simulation Period 1 m imposing measured data

(c) UB flow simulation Period 1 m measured data can change 10 %

(d) UB flow simulation Period 0.005 m

(e) UB flow simulation Period 0.005 m imposing measured data

(f) UB flow simulation Period 0.005 m measured data can change 10 %

Figure 3.12: Results cross section elimination staggered case

DETAILED LOOK ON SOME SPECIFIC PART OF THE FLUME

So far; the average behavior of the system has been analyzed, now some detailed velocities data are depicted. The first case to be analyzed is when all the data from the CFD is used as input of the model (Figure 3.14 the black vertical lines represents the intrusion position). Figure 3.14 show node velocities U (U_x,U_y,U_z) at a certain x, y position, but following z coordinate (Figure 3.13) . Figure 3.14(a) shows the y components of the velocity, its approximation is good until reach the intrusion. After the intrusion, the data from the CFD based interpolation methodology differ from the original data. This can be caused by the no representation of a physical phenomena combined with the order of magnitude. Figure 3.14(b) is the cross sectional velocity, the approximation with the CFD based methodology is much better, but in some points the velocity is underestimated. Figure 3.14(c) show the stream wise component of the velocity. This velocity has the biggest order of magnitude. The Figure shows a good approximation of this velocity component.

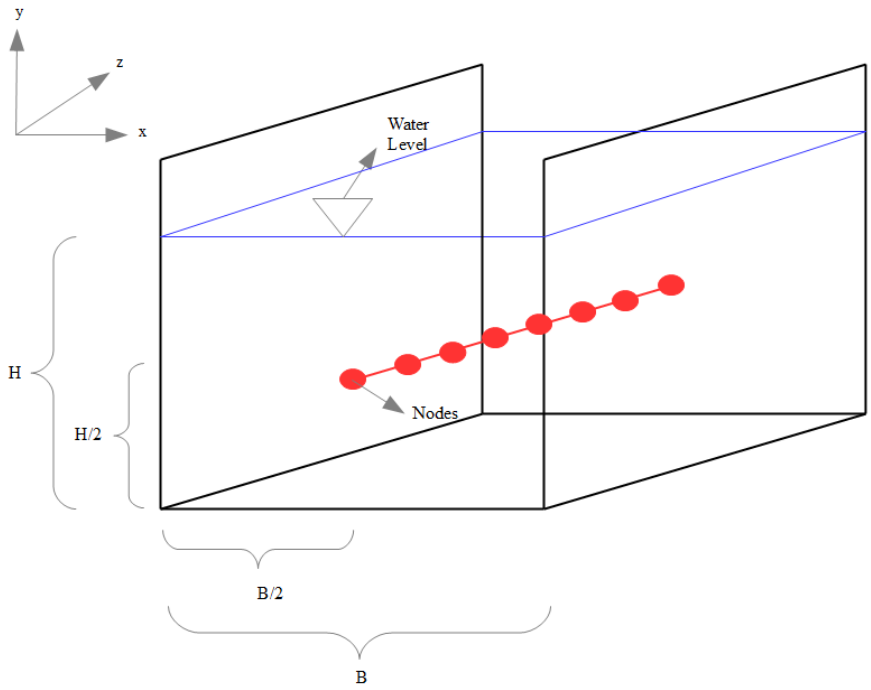

Figure 3.13: Location of nodes data to be analyzed

Hereafter, the scenarios data sampling are analyzed for the case when data measured cannot be modified. Figure 3.15 depicts the velocity components when cross sections are removed. Figure 3.15(a) shows the velocity in y direction, data which is no measured has a great variation with an order of magnitude higher than measured velocities. Figure 3.15(b) is the cross sectional velocity component which provides better results, but in some points such as in section 20 there is a sudden change in the sign of the slope (oscillation). Figure 3.15(c) represents the main component of the velocity, this Figure depicts some problems where the values are not fixed (no measured data). A conclusion can be drawn of this analysis: If some data is forced other data have to compensate the gradients in all the directions, as a consequence the data can make no sense or oscillate to compensate gradients. A smooth result is found when there is no data forcing.

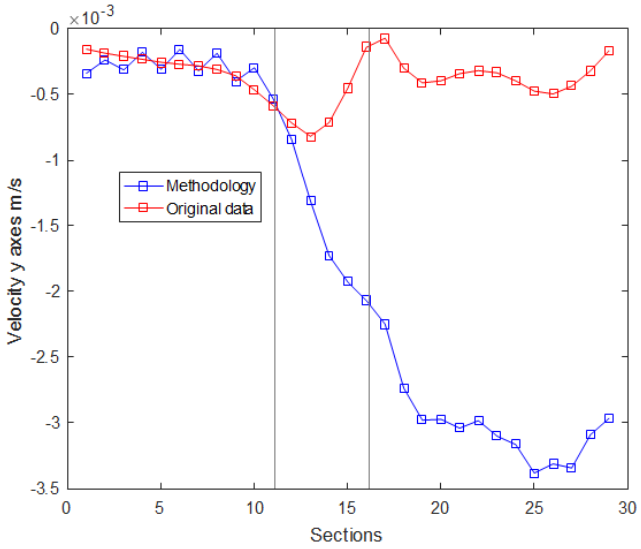

(a) Velocities in y direction

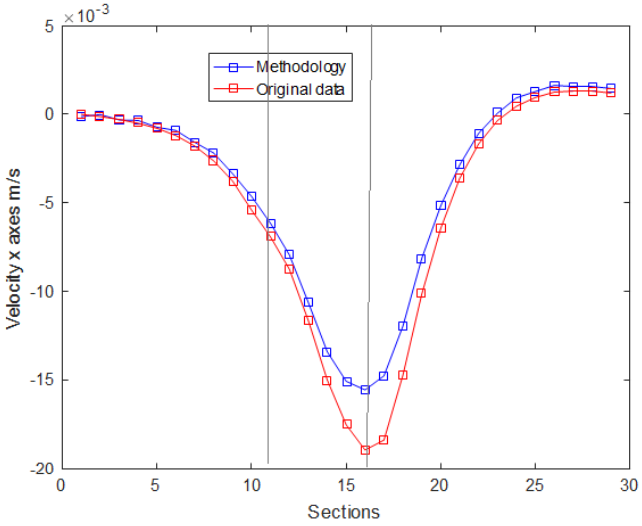

(b) Velocities in x direction

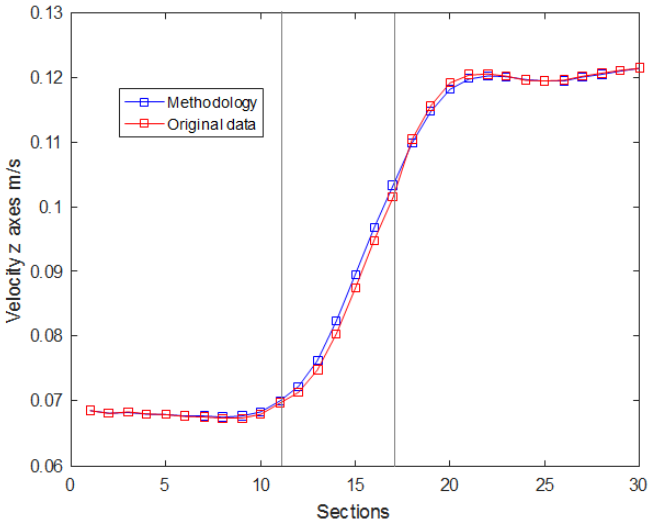

(c) Velocities in z direction

Figure 3.14: Velocities components when the whole CFD data are used

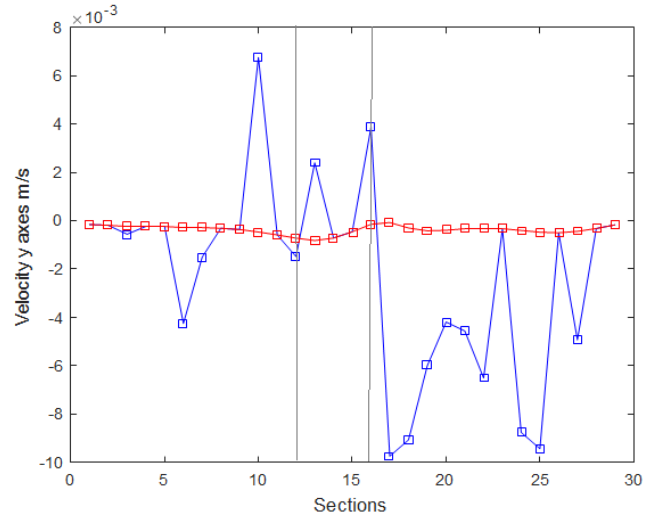

(a) Velocities in y direction

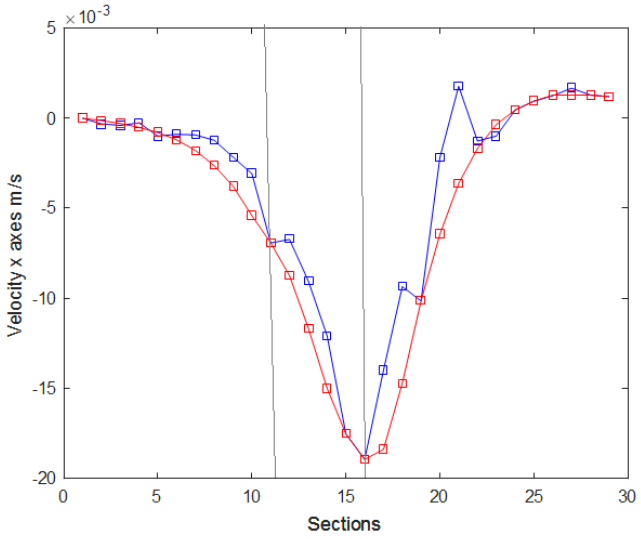

(b) Velocities in x direction

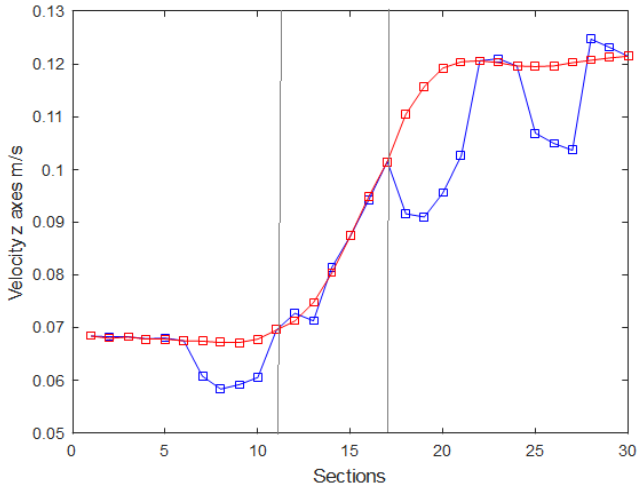

(c) Velocities in z direction

Figure 3.15: Velocities components with cross section withdrawing

CFD DATA INCLUDING LATERAL CONNECTION DATA

The whole system (including the intrusion flume) was modelled in order to test the CFD based interpolation methodology whether can be used to simulate an intersection or not. Figure 3.16 show the result of the simulations for two grid systems: one with coarse grid ($\Delta x = 0.1m, \Delta y = 0.03m, \Delta z = 0.1m$) (Figures 3.16(a) and 3.16(b)) and another with finer grid ($\Delta x = 0.05m, \Delta y = 0.03m, \Delta z = 0.05m$) (Figures 3.16(c) and 3.16(d)). Figures 3.16(a) and 3.16(c) depicts the mean flow in the main flume. The section number increase downstream. The CFD based interpolation methodology results are good even with the coarser grid (Figure 3.16(a)) and they improve with a finer grid (Figure 3.16(a)). Figures 3.16(b) and 3.16(d) depicts the mean flow of the intrusion. The sections increase downstream of the intrusion, so the final section is the point where the main flume intersects the intrusion. In this case, the coarse grid have troubles to predict the behavior at the intersection (Figure 3.16(b)), on the other hand when grid is refined there is a better approximation. However, near the intersection there is instabilities in the prediction, it could be possible that a physical phenomena such as turbulence is not well represented in that point (Figure 3.16(d)).

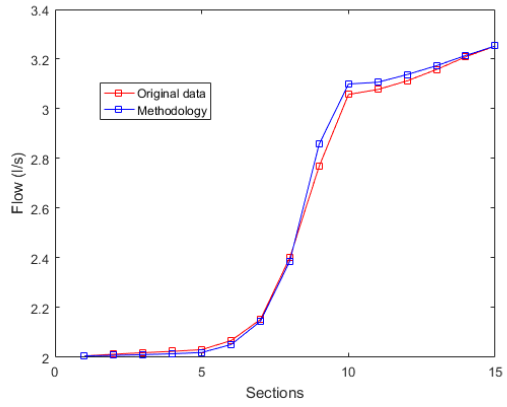

(a) Mean flow main flume coarserr grid

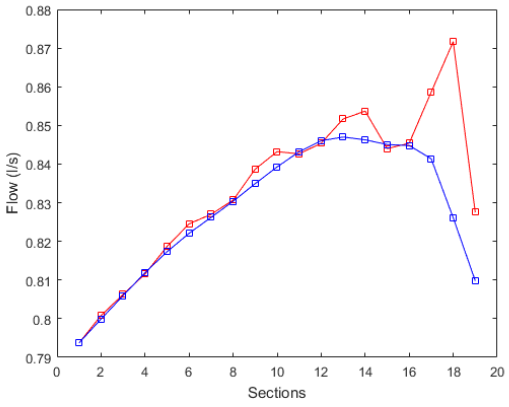

(b) Mean flow intrusion coarser grid

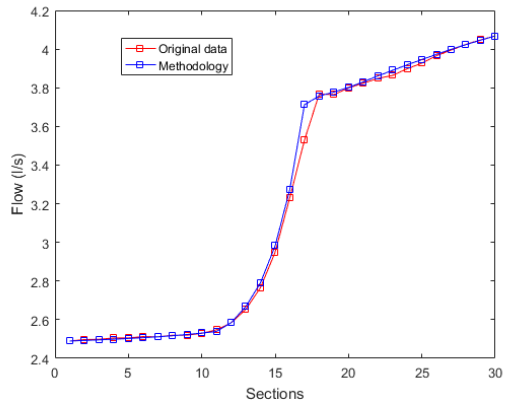

(c) Mean flow main flume finer grid

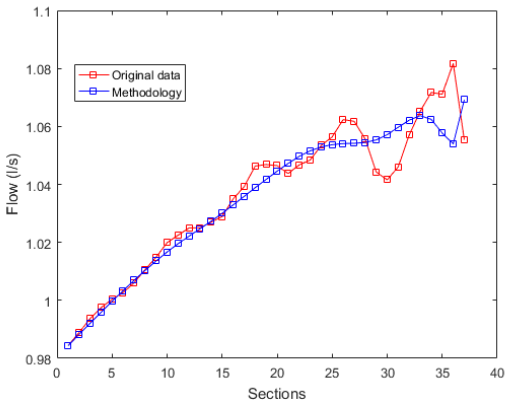

(d) Mean flow intrusion finer grid

Figure 3.16: Mean flow system including intrusion data

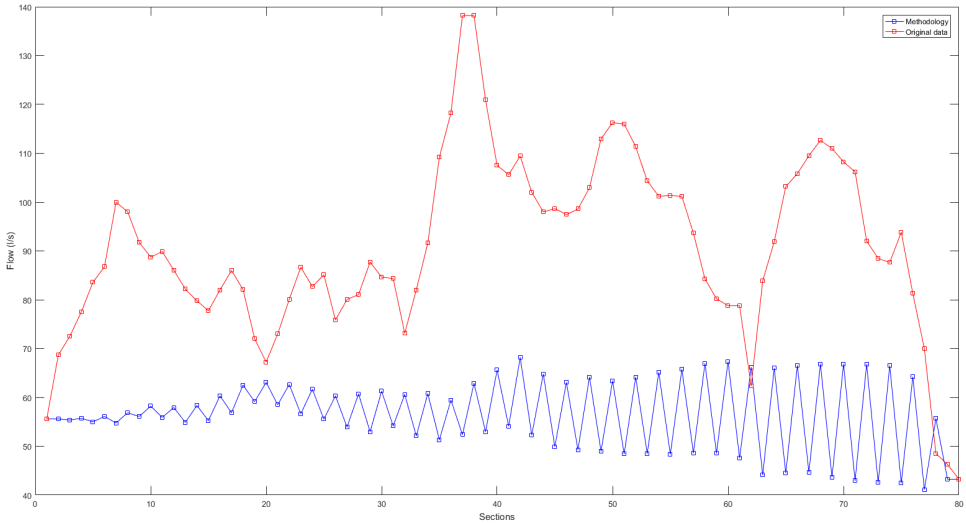

Figure 3.17: UB flow non staggered grid system

3.3. UB FLOW DATA RESULT

After the validation of the proposed methodology (CFD data), the method was tested on experimental data. The UB flow provides with 1-D velocity, but 3D velocity field was obtained based on some formulation from the manufacturer and the application of Section 2.2.4. Figure 3.17 depicts the result for non-staggered grid, this Figure shows the mean flow in the cross section (numeration of cross section increase up stream), results show the oscillations in this system. Moreover, the methodology did not converge and the system had to be stopped since the tolerance start to oscillate from 50 to 100 %.

Figure 3.18 depict the results of the staggered grid, there is a better behavior of the system after the methodology converges, but the converged system present an incorrect behavior.

The cause of this not good result could be due to the raw data , if it is analyzed the vertical component of the velocity in the UB flow data is one degree higher in comparison with the main component than in the CFD data taking the same comparison. Since 3 D data is necessary and UB flow provides 1 D data, an adjustment to configuration or operation will be necessary. To use the CFD based interpolation methodology a device able to measure 3 D velocities is necessary in order to be able to test the methodology with real data. This methodology is based on gradients, so the initial values must have physical sense to correct the remaining of data. In this case unfortunately there is uncertainty about the UB flow data and the components calculated.

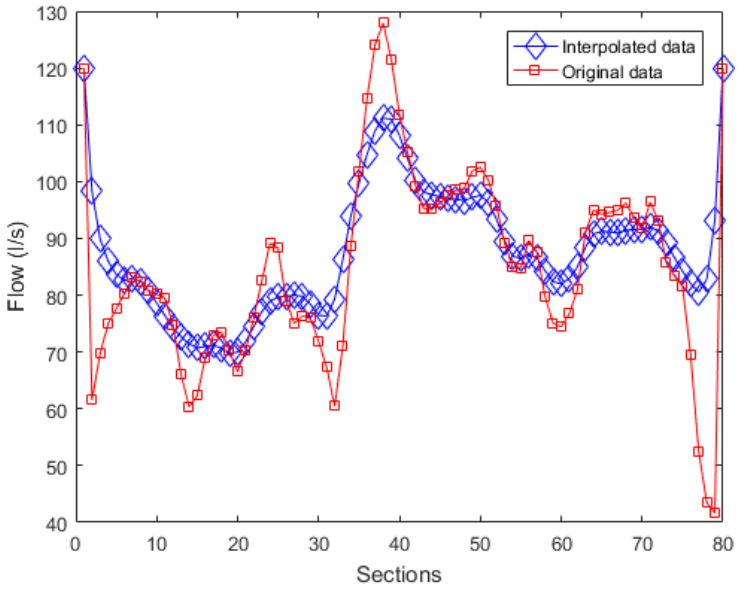

Figure 3.18: UB flow staggered grid

3.4. DISCRETIZATION STABILITY ANALYSIS

3.4.1. DISCUSSION SCHEMES STABILITY

The possible roots for different discretizations schemes have been calculated. The scheme presented in subsection 2.3.1 is a non-staggered grid which first derivatives are analyzed in $i+1$ and $i-1$. It represents the easiest centered discretization case. Even thought this approximation was not used during this thesis, its result was consider interesting to test the pressure weighted interpolation of [23] (Scheme used during non-staggered test). The characteristic equation roots were -1 and 1. Roots were independent of Δx or Δt. Besides, the approximation shows an important difference with the findings of [29] for a Preissmann scheme. Preissman stability depends on the discretisation in time and space.

Subsection 2.3.2 is the non-staggered scheme used in this thesis based on recommendation of [16]. For this scheme the characteristic root can be -1 under the condition r=-1. Hence, the pressure weighted interpolation propose by [23] increases the stability of the system, but there is still possibility of oscillation.

Subsection 2.3.3 shows a staggered scheme. The characteristic equation root is 1, so the scheme is stable.

4

CONCLUSION AND PERSPECTIVES

This work presented two main objectives: i) the study of the UB capabilities to measures 3D velocity field and ii) the adaptation of the method proposed by [16] in order to identify and lateral connection. Despite numerous experiments and rather overall good averaged velocity (i.e. consistent with the hydraulic conditions), the UB flow (in its actual version) seems to be not suitable for such purpose. The observed oscillations from the average velocity along the flume are independent of the rotation and translation movement of the profiler: further investigations are required to understand this behavior (present in every experiment). However, the proposed methodology reaches the initial goals with proper data (obtained from a CFD simulation): the 3D interpolation method, based on hydraulic equations, delivers an accurate knowledge on the velocity distribution along the reach and, consequently, the quantification and identification of the lateral connection.

In order to fulfill the expected functions of the FOULC project, some serious improvements on the UB Flow are necessary: i) a simultaneous measurement on both transducers, ii) an auto-adaptative configuration with the hydraulics conditions (water depth, velocity range) and iii) a better orientation of the Tr3 (results are quite sensitive to the 97 degrees angle). Furthermore, the derivation of the 3D velocity from the 2D one given the UB Flow and its rotation is too uncertain.

Regarding the 3D interpolation method, the staggered grid highlights once again its higher performance by comparison to the non-staggered one: no oscillations occur. The adaptation of the discretization scheme done by [23] shows an improvement but still presents some oscillations in some specific condition: this method appears not suitable for an end-user application. Unfortunately, the results of the different subsampling data scenarios show the rather strong effect of the first interpolation step (to fulfill the grid). Furthermore, any explanation has been yet found for the strange behavior in the interpolated vertical velocities (Figure 3.14(a)): some additional experiments or simulations seem necessary, while varying the discharge ratio between the lateral and the main pipes. This methodology is based on velocity and pressure gradients and depending on their orders of magnitude: noise or measurement errors can have significant impacts in the methodology, especially for low velocity and low ratio lateral/main pipe discharges. Some numerical tricks (e.g. by changing velocity units) may do this method more robust for such conditions.

The application in the FOULC project will need a code able to detect the cross connection in the velocity data: velocity distribution issued from the lateral pipe needs to be set up as boundary conditions during the fourth step the proposed methodology. That's why a detection algorithm for lateral connection detection needs to be implemented. Analyzing the velocities components at the walls looking for irregularities can do detection.

A

Detection Methodologies

Table A.1: Methodologies for sewer systems assessment

Type	Methodology	Description	Drawback	References
Sensor Evaluation	Visual Inspection	The most widely used methodology is Closed Circuit TV. This methodology is based on the appreciation of the general appearance of the pipe which is captured in video and analyzed afterwards	Subjective due to dependence on technical expertise as well as CCTV image	[3] [33]
Sensor Evaluation	Dye Testing	To put a tracer in the toilet and flush the toilet	Requires access to private properties and time consuming	[3] [5]
Sensory Evaluation	Smoke testing	Same as dye testing but instead of a tracer it is used smoke	Methodology most used to detect when storm water is connected to sewer system	[3]
Sensor Evaluation	Sonic Distance measurement method	Based on the traveling time of a burst from the origin to a target. The sound velocity changes depending on the material. It is possible to know the pipe deflection, and corrosion.	It cannot operate in both air and water since it requires different equipment. Thus , the sewer system must be empty	[33]
Sensory Evaluation	Another Acoustic Method	This methodology is based on the use of microphones to get the temporal and frequency characteristics in the behavior if acoustic intensity. It can detect lateral connections	Laboratory scale	[34]
Sensor Evaluation	Use of lasers	This method is based on the use of laser scanning to measure the interior geometry of a pipe.	Due to the random nature of cross connections it could not be able to detect them	[6]
Combination of sensors	KARO-PIRAT-SSET	System with multiple sensor and cameras. The goal is to provide to the Engineer with a higher amount and quality data.	They are expensive	[33]
Method using indicators	Temperature	The ewer system have a different temperature than storm water. One example of this methodology is the use of distributive temperature sensing (DTS)	In case of DTS there are effects of raining in the temperature which have the same effect as cross connections	[5]

Table continuation				
Type	Methodology	Description	Drawback	References
Method using indicators	Aerial infrared photography	Measure the temperature at storm outlet	Expensive equipment	[3]
Method using indicators	Chemical Parameters	Measure of conductivity, Caffeine , nutrients	Some of them are not conservative, and for others the analysis cost is too high.	[3]

BIBLIOGRAPHY

[1] D. Butler and J. Davies, *Urban drainage* (CRC Press, 2004).

[2] E. Kuliczkowska, *Analysis of defects with a proposal of the method of establishing structural failure probability categories for concrete sewers,* Archives of Civil and Mechanical Engineering **15**, 1078 (2015).

[3] O. Panasiuk, A. Hedström, J. Marsalek, R. M. Ashley, and M. Viklander, *Contamination of stormwater by wastewater: A review of detection methods,* Journal of environmental management **152**, 241 (2015).

[4] R. Fenner, *Approaches to sewer maintenance: a review,* Urban water **2**, 343 (2000).

[5] O. Hoes, R. Schilperoort, W. Luxemburg, F. Clemens, and N. Van De Giesen, *Locating illicit connections in storm water sewers using fiber-optic distributed temperature sensing,* water research **43**, 5187 (2009).

[6] F. Clemens, N. Stanić, W. Van der Schoot, J. Langeveld, and M. Lepot, *Uncertainties associated with laser profiling of concrete sewer pipes for the quantification of the interior geometry,* Structure and Infrastructure Engineering , 1 (2014).

[7] U. S.A.S., *UB-Flow profiler-User Manual*, 4 rue Boussingault (2005).

[8] K. Makris, *Detection and quantification of lateral, illicit connections and infiltration in sewers with Infra-Red camera: conclusions after a wide range of experiments*, Master's thesis (2016).

[9] S. Sun, H. Yan, and G. L. Kouyi, *Artificial neural network modelling in simulation of complex flow at open channel junctions based on large data sets,* Environmental Modelling & Software **62**, 178 (2014).

[10] H. Brito, Jose, R. Angst, K. Koser, and M. Pollefeys, *Radial distortion self-calibration,* in *Proceedings of the IEEE Conference on Computer Vision and Pattern Recognition* (2013) pp. 1368–1375.

[11] V. Chari and A. Veeraraghavan, *Lens distortion, radial distortion,* in *Computer Vision: A Reference Guide*, edited by K. Ikeuchi (Springer US, Boston, MA, 2014) pp. 443–445.

[12] MathWorks, *What is camera calibration?* (2016).

[13] N. Stanić, F. Clemens, M. Catieau, J. Langeveld, and M. Lepot, *A new and collaborative technology for sewer pipe inspection (part 1): design, ccalibrations, corrections and potential application of a laser profiler,* (2016).

[14] D. Gruber, *The mathematics of the 3d rotation matrix,* in *The Xtreme Game Developers Conference* (2000).

[15] U. de Las Palmas de Gran Canaria, *Tema 4: Transformaciones 3d,* (2015).

[16] R. Tsubaki, Y. Kawahara, Y. Muto, and I. Fujita, *New 3-d flow interpolation method on moving adcp data,* Water Resources Research **48** (2012).

[17] F. Moukalled, L. Mangani, and M. Darwish, *The Finite Volume Method in Computational Fluid Dynamics* (Springer, 2016).

[18] J. McDonough, *Lectures in elementary fluid dynamics: Physics, mathematics and applications,* University of Kentucky, Lexington (2004).

[19] J. H. Ferziger and M. Peric, *Computational methods for fluid dynamics* (Springer Science & Business Media, 2012).

[20] H. G. Im, *Numerical methods for the navier-stokes equations,* (2001).

[21] J. B. Perot, *An analysis of the fractional step method,* Journal of Computational Physics **108**, 51 (1993).

[22] J. H. Ferziger and M. Peric, *Computational methods for fluid dynamics* (Springer Science & Business Media, 2012).

[23] S. W. Armfield, N. Williamson, M. Kirkpatrick, and R. Street, *A divergence free fractional step method for the navier-stokes equations on non-staggered grids,* ANZIAM Journal **51**, 654 (2010).

[24] S. Abdallah, *Numerical solutions for the pressure poisson equation with neumann boundary conditions using a non-staggered grid, i,* Journal of computational physics **70**, 182 (1987).

[25] S. Abdallah, *Numerical solutions for the incompressible navier-stokes equations in primitive variables using a non-staggered grid, ii,* Journal of computational physics **70**, 193 (1987).

[26] F. Sotiropoulos and S. Abdallah, *The discrete continuity equation in primitive variable solutions of incompressible flow,* Journal of Computational Physics **95**, 212 (1991).

[27] P. M. Gresho and R. L. Sani, *On pressure boundary conditions for the incompressible navier-stokes equations,* International Journal for Numerical Methods in Fluids **7**, 1111 (1987).

[28] M. Griebel, T. Dornseifer, and T. Neunhoeffer, *Numerical simulation in fluid dynamics: a practical introduction*, Vol. 3 (Siam, 1997).

[29] F. H. L. R. Clemens, *Hydrodynamic models in urban drainage application and calibration* (TU Delft, Delft University of Technology, 2001).

[30] D. Gonze, *Linear difference equations,* (2012).

[31] R. Godunov, *Theory of difference schemes-an introduction,* Amsterdam: North Holland, 1964 (1964).

[32] J. Battjes and R. Labeur, *Lecture notes on Open Channel Flow*, Tech. Rep. (TU Delft, 2014).

[33] R. Wirahadikusumah, D. M. Abraham, T. Iseley, and R. K. Prasanth, *Assessment technologies for sewer system rehabilitation,* Automation in Construction **7**, 259 (1998).

[34] F. Zao, K. V. HOROSHENKOV, M. T. B. ALI, and J. Simon, *An acoustic method for condition classification in live sewer networks,* (2012).